



Deposited via The University of Leeds.

White Rose Research Online URL for this paper:

<https://eprints.whiterose.ac.uk/id/eprint/106864/>

Version: Accepted Version

---

**Article:**

Frischbutter, AA, Fisher, QJ, Namazova, G et al. (2017) The value of fault analysis for field development planning. *Petroleum Geoscience*, 23 (1). pp. 120-133. ISSN: 1354-0793

<https://doi.org/10.1144/petgeo2016-053>

---

© 2016 The Author(s). Published by The Geological Society of London for GSL and EAGE. This is an author produced version of a paper published in *Petroleum Geoscience* 23(1):120-133 Feb 2017; <https://doi.org/10.1144/petgeo2016-053>. Uploaded in accordance with the publisher's self-archiving policy.

**Reuse**

Items deposited in White Rose Research Online are protected by copyright, with all rights reserved unless indicated otherwise. They may be downloaded and/or printed for private study, or other acts as permitted by national copyright laws. The publisher or other rights holders may allow further reproduction and re-use of the full text version. This is indicated by the licence information on the White Rose Research Online record for the item.

**Takedown**

If you consider content in White Rose Research Online to be in breach of UK law, please notify us by emailing [eprints@whiterose.ac.uk](mailto:eprints@whiterose.ac.uk) including the URL of the record and the reason for the withdrawal request.

1                                   **The value of fault analysis for field development planning**

2           Andreas A. Frischbutter<sup>1\*</sup>, Quentin J. Fisher<sup>2</sup>, Gyunay Namazova<sup>1</sup> & Sebastien Dufour<sup>1</sup>

3  
4                                   <sup>1</sup>*Wintershall Norge AS, Laberget 28, 4020 Stavanger, Norway*

5                                   <sup>2</sup>*School of Earth and Environment, University of Leeds, Leeds, LS2 9JT, UK*

6                                   \**Corresponding author (Andreas.Frischbutter@wintershall.com)*

7  
8           Work carried out at **Wintershall Norge AS** and **Center for Integrated Petroleum Geoscience,**  
9                                   **University of Leeds**

10  
11                                   **Abbreviated title:** *Fault analysis in field development planning*

12  
13   **Abstract:** Faults play an important role in reservoir compartmentalization and can have a significant impact  
14 on recoverable volumes. A recent petroleum discovery in the Norwegian offshore sector, with an Upper  
15 Jurassic reservoir, is currently in the development planning phase. The reservoir is divided into several  
16 compartments by syn-depositional faults that have not been reactivated and do not offset the petroleum-  
17 bearing sandstones completely. A comprehensive fault analysis has been conducted from core to seismic  
18 scale to assess the likely influence of faults on the production performance and recoverable volumes. The  
19 permeability of the small-scale faults from the core were analyzed at high confining pressures using  
20 formation compatible brines. These permeability measurements provide important calibration points for the  
21 fault property assessment, which was used to calculate transmissibility multipliers (TM) that were  
22 incorporated into the dynamic reservoir simulation model to account for the impact of faults on fluid flow.  
23 Dynamic simulation results reveal a range of more than 20% for recoverable volumes depending on the  
24 fault property case applied and for a base case producer/injector well pattern. The fault properties are one  
25 of the key parameters that influence the range of cumulative recoverable oil volumes and the recovery  
26 efficiency.

27  
28   **Keywords:** fault property analysis, fault permeability prediction, fault rock petrophysics, transmissibility  
29 multiplier, dynamic reservoir simulation, field development planning

30

## 31 **Introduction**

32 A recently discovered oil field with a gas cap in the Norwegian offshore sector is currently in the  
33 development planning phase. Four exploration/appraisal wells have been drilled in the field, but no  
34 production data exists at this stage of the field lifecycle. Key uncertainties that impact recoverable volumes  
35 and production behaviour range from reservoir distribution (i.e. sedimentologically-controlled  
36 compartmentalization), reservoir properties, fault architecture and fault rock properties. In terms of the  
37 latter, the field is compartmentalized by numerous faults at the seismic scale, but also contains numerous  
38 sub-seismic scale faults. An understanding of the fault properties and their influence on the field production  
39 and recoverable volumes is essential for assessing the fields economics, planning a production strategy and  
40 also influences the design of the facilities. In this paper we focus on the impact of structural pattern and  
41 fault rock properties on the subsurface fluid flow and hence the production.

42 Workflows exist for the quantitative assessment of the impact of faults on fluid flow in petroleum  
43 reservoirs and can be implemented using a range of software tools that are commonly available (see review  
44 by Fisher & Jolley, 2007). In general, the workflow begins by undertaking a structural analysis using  
45 seismic data. Faults identified from seismic are then incorporated into the geological model. The clay  
46 distribution along the faults is then estimated using well established algorithms. In siliciclastic reservoirs,  
47 the main fault seal processes are: (i) cataclasis; (ii) mixing of clays with framework grains, (iii) clay smear,  
48 and (iv) post-deformation diagenesis such as quartz cementation and grain-contact quartz dissolution  
49 (Fisher and Knipe, 1998; 2001). The presence of clay is important for two of these mechanisms which often  
50 results in correlations between fault permeability and clay content; these correlations may then be used to  
51 calculate transmissibility multipliers (TM) that are incorporated into simulation models to take into account  
52 the impact of faults on fluid flow. Fault rock permeability data can be obtained from global datasets.  
53 However, some studies suggest that better results are obtained if fault permeability estimates are based on  
54 the laboratory measurements made on fault rocks sampled from cores taken within the field being appraised  
55 or from nearby analogues (Fisher & Knipe, 2001; Sperrevik *et al.*, 2002; Jolley *et al.*, 2007).

56 The study reported in this paper follows the general workflow described above. A key difference, however,  
57 is that many fault compartmentalization studies use fault rock property data that was collected under  
58 inappropriate laboratory conditions. For example, many studies use fault rock permeability data collected  
59 at ambient confining pressures using brine compositions that are not compatible with the formation despite  
60 a wealth of evidence to suggest that the permeability of tight rocks is very sensitive to the stress conditions  
61 (e.g. Thomas and Ward, 1972) and the brine chemistry (e.g. Lever and Dawe, 1987). The current study  
62 differs in that fault rock permeability measurements were made at high stresses using formation compatible

63 brines. The new fault rock permeability data has then been incorporated into the dynamic reservoir  
64 simulation model to improve production forecasts.

65

## 66 **Reservoir**

67 The main reservoir is in Late Jurassic sandstones of the Heather Formation. The reservoir is  
68 comprised of turbiditic sandstones, deposited syntectonically, during the main rifting event in the  
69 Late Jurassic. The reservoir is currently located at a depth between 2400m – 2800m, with the  
70 temperature at reservoir level being slightly above 90° C. Glacial melting during Pleistocene  
71 times resulted in an uplift of approximately 300m. The reservoir thickness varies between 10m  
72 and 130m (mean 60m). The N/G of the reservoir section varies between 55% and 73%. The  
73 reservoir permeabilities range from 0.1 – 5 Darcy and porosities vary between 10% and 30%.  
74 The reservoir experienced the precipitation of early K-feldspar overgrowths and kaolin during  
75 shallow burial. Mechanical compaction was the main process for reducing porosity and  
76 permeability during intermediate burial. The sandstones experienced small amounts of quartz  
77 precipitation and grain contact quartz dissolution during deep burial.

78

## 79 **Structural setting**

80 The field is compartmentalized by numerous seismic scale, mainly NW-SE and NE-SW striking, normal  
81 faults (Fig. 1a). East-West striking faults are present, but to a minor amount. The maximum fault throw  
82 observed is around 60m with a mean around the seismic resolution of 25m. The main reservoir is self-  
83 juxtaposed throughout the field (Fig. 1b), implying that the properties of the fault rocks need to be  
84 considered to predict the impact of faults on fluid flow during production. It is important to note that no  
85 evidence of a static fault seal over geological time exists within the main part of the field. The wells drilled  
86 in the main part of the field, e.g. well A, B, D, have pressures on a common gradient, which is consistent  
87 with communication through the hydrocarbon phase. However, this cannot be taken as evidence that the  
88 faults will not impact flow on a production time-scale. The hydrocarbon water contact has been drilled in  
89 well B, whereas the wells A and D have an oil- and gas-down-to.

90 Deposition of the reservoir happened syntectonically and the turbidites were deposited in half grabens (Figs  
91 2, 3). Faulting started in the Late Triassic and continued throughout the Early and Middle Jurassic, with the  
92 main rifting in the Late Jurassic. In general, the tectonic activity ceased in the Latest Jurassic, but some

93 faults are active in the Early Cretaceous (Fig. 2). Structural restoration indicates that the faulting that  
94 affected the reservoir occurred at relatively shallow depths (<1000m).

95 The main fault network only represents faults that could be mapped over a larger distance and continuously  
96 on seismic sections. It shall be pointed out that the seismic quality, even after reprocessing is only fair to  
97 poor in the field area, which adds uncertainties to the fault interpretation. The intensity of seismic scale  
98 faulting differs around the four wells (well A = 4 faults/km<sup>2</sup>, well B = 2 faults/km<sup>2</sup>, well C = 4 faults/km<sup>2</sup>,  
99 well D = 1 fault/km<sup>2</sup>). Seismic attribute analysis (ant-tracking, Fig. 4) in combination with core and  
100 borehole image analysis data (Fig. 5a) suggest a denser fault network (well A = 2 faults/km<sup>2</sup>, well B = 10  
101 faults/km<sup>2</sup>), which is not represented by a visible offset of horizons at the current seismic resolution. Well  
102 A drilled right through one of the faults identified on seismic attribute analysis (Fig. 4). Plotting fault zones  
103 identified from borehole image analysis on seismic sections at the well location indicates that many small  
104 scale faults are only subtle or not at all visible on the seismic (Fig. 5b). Similar features as in well A are  
105 also observed in well B. Very few small-scale faults are recorded in borehole image logs and cores in the  
106 southern well C and D at the reservoir level, although those are also located very close to seismic scale  
107 faults. No reliable results from the attribute analysis could be obtained due to the poorer quality of the  
108 seismic around the two wells.

109

## 110 **Fault rock property analysis**

### 111 **Fault rock samples**

112 The complete reservoir section has been cored in the wells A and B and the samples analysed in this study  
113 were taken entirely from these two cores. Two fault zones with unknown offsets are visible in well A (Fig.  
114 6, see also Fig. 5a). It seems appropriate to expect similar fault styles observed in the fault rock samples  
115 also at a larger scale in the reservoir-scale faults. Figure 7a shows multiple faults on a small scale, which  
116 reflects the observations made on the seismic and borehole images. The fault propagates upwards,  
117 nucleating at the lower left and fault splays are developed in the more shale-rich section (between 37m and  
118 33cm). The fault continues with a clearly visible offset of a distinctive shale band (29cm). A small clay  
119 smear is developed, resulting from the smearing of the fine clay-rich laminations within the sand-rich  
120 interval. In the clean sandstones above and below the clay-rich band, the clay content of the fault rock  
121 seems to be significantly lower. This is likely to represent the fault rock properties expected in the self-  
122 juxtaposed cleaner sandstones section for the reservoir scale faults. A small half-graben is present towards  
123 the top of Figure 7a, which is infilled with coarser material. The cored faults in more shale-rich layers often  
124 show partial clay smear, or at least a clay-rich fault rock (Fig. 7b, c). It is, however, apparent from the

125 sampled faults that clay smears are often discontinuous. It is occasionally observed that the fault dip flattens  
126 in the more shale-rich lithologies at the seismic scale (Fig. 3). The same phenomena, caused by  
127 geomechanical heterogeneities, is also observed at a small scale in the cored faults, where the dip of the  
128 fault surface becomes less steep in the more clay-rich layers (Fig. 8a). Deformation bands are commonly  
129 observed features and the fact that no grain fracturing has occurred during faulting indicates that they were  
130 formed during shallow burial (Fig. 8b, c).

131 A bias exists for the fault rock samples. In the more heterogeneous section the sample integrity has been an  
132 issue, so only faults in the more homogenous, sandier section could be sampled. This implies that faults in  
133 impure sandstones and in clay-rich layers are under-represented.

134

### 135 **Analytical procedures**

136 Extensive laboratory work was undertaken on selected fault rock samples from two wells (A & B) including  
137 CT-scanning, SEM-analysis, absolute permeability analysis, and quantitative XRD (QXRD). The  
138 individual techniques are described in more detail below.

#### 139 *Sample preparation*

140 Typically, 10 to 20 cm sections of core containing the faults were carefully wrapped and sent to the  
141 laboratory for analysis. On arrival, the samples were photographed and CT scans were taken using a Picker  
142 PQ 2000 medical-style scanner to identify the orientation of faults present and whether or not there were  
143 obvious signs of damage generated during coring or following coring. The CT scans allowed us to identify  
144 the optimal orientations to take samples for further analysis. A range of subsamples were required for  
145 microstructural and petrophysical property analysis of the fault rock present and its associated undeformed  
146 sandstone including:-

147 • Core plugs of the host and fault rock; the latter were orientated perpendicular to the fault so that  
148 fluid was forced to flow across the fault during analysis. It is generally preferred to take 25.4 or  
149 38.1 mm core plugs but the core was too thin so 16 and 20 mm core plugs were taken and these  
150 were analysed in purpose built core holders.

151 • Cubes of fault rock and host sandstone, around 1 to 1.5 cm<sup>3</sup>, were cut for permeability analysis.  
152 The sample containing the fault rock were cut and set in dental putty in an orientation that meant  
153 that fluid had to flow through the fault rock during permeability analysis. The use of dental putty  
154 means that it is not possible to apply high confining pressures to these samples during permeability  
155 analysis.

- 156       • Around 1.5 x 1.5 x 0.5 cm samples containing fault rock and the associated host sandstone were  
157       cut for microstructural analysis.
- 158       • A 1cm<sup>3</sup> sample representative of the host sandstone was then taken for QXRD analysis. This  
159       analysis was not performed on the fault rocks as they were too narrow to be sampled. The fault  
160       throws are very low so it was assumed that the mineralogy of the fault is the same as the host  
161       sandstone, which is consistent with microstructural observations.

162 All samples were cleaned in a Soxhlet extractor using a 50:50 mixture methanol-toluene/dichloromethane  
163 and then dried in a humidity controlled oven at 60°C.

#### 164 *SEM analysis*

165 The blocks for microstructural analysis were impregnated with a low viscosity resin, ground flat with  
166 progressively finer grades of diamond culminating in a polish using 1 µm diamond paste. The samples were  
167 then coated with a 10 nm thick layer of carbon before being analysed using a FEI Quanta 650 FEGSEM  
168 environmental SEM with Oxford Instruments INCA 350 EDX system/80mm X-Max SDD detector, EBSD  
169 and KE Centaurus EBSD system. The mineralogy and diagenetic history of the samples was determined as  
170 well as the fault rock microstructure and timing of faulting relative to the diagenetic history. BSEM images  
171 were stored as 8 bit TIFF files so that they could be incorporated into an image analysis package and their  
172 mineralogy quantified.

#### 173 *Permeability analysis*

174 Permeability measurements were made using two methods. One set of measurements were made at ambient  
175 stress using distilled water as the permeant so the results could be compared to those from previous studies  
176 of the permeability of fault rocks (e.g. Fisher & Knipe, 1998; 2001). In these cases, the cleaned cubes were  
177 set in dental putty so that they could be confined at 70 psi confining pressure in a steady-state water  
178 permeameter. The samples were saturated with distilled water, placed in the permeameter before using  
179 syringe pumps to establish steady-state flow. The permeability was calculated using Darcy's law based on  
180 the flow rate, sample length and area, the upstream and downstream pressure differential and the viscosity  
181 of the water. The samples containing fault rock also contained undeformed sandstone so the fault  
182 permeability was deconvolved from the measurements assuming that the permeability measured was the  
183 thickness weighted harmonic average of the fault rock and the host sediment.

184 The second set of measurements were made on core plugs at higher stresses using formation compatible  
185 brine. Coreholders were specially constructed for the sample analysis as we could only obtain 16 and 20  
186 mm diameter core plugs, which are far narrower than the 25.4 and 38.1 diameter cores normally analysed.  
187 The core plugs were trimmed so that the ends were flat and orientated perfectly perpendicular to the axis

188 of the core plug. Formation compatible brine permeabilities were measured under stresses of 500psi, 1500  
189 psi, 2000psi, 2500psi, 3000psi, 4000psi, 5000psi. These high stresses close microfractures created as core  
190 samples are brought to the surface following coring. Samples with permeabilities of >0.1 mD were  
191 measured using the steady-state technique whereas samples with lower permeabilities were measured using  
192 the pulse-decay method. As with ambient stress measurements, core plugs containing fault rock also  
193 contained undeformed sandstone so the fault permeability was deconvolved from the measurements  
194 assuming that the permeability measured was the thickness weighted harmonic average of the fault rock  
195 and the host sediment.

#### 196 *QXRD analysis*

197 The intensity of a X-ray diffraction pattern of a mineral is proportional to the amount present within a  
198 mixture (e.g. Hardy & Tucker, 1988). On this basis, XRD has frequently been used to quantify the  
199 proportions of minerals present within rocks. One method to make such analyses is to construct calibration  
200 curves based on the XRD analysis of mixtures containing different proportions of an internal standard such  
201 as corundum. The technique requires preparation of samples with complete random orientation (Brindley,  
202 1984). Sample preparation has, however, proved such a difficult task that the technique has been widely  
203 regarded as semi-quantitative at best (Hillier, 1999). Recently, a spray dry technique has been developed  
204 that appears to produce samples for XRD analysis without significant preferred orientation - even when  
205 they contain significant proportions of clays (Hillier, 1999; 2000). The technique involves grinding the  
206 sample with a standard (20 wt. % corundum) and then spraying a slurry of the mixture through an air brush  
207 into a tube furnace to form ~30 µm wide spherical aggregates with random mineral orientation. The spheres  
208 are then top loaded into a specimen holder and then analysed using XRD. The diffraction results obtained  
209 are analysed by either reference intensity ratio (RIP) or a Rietvold method to produce mineralogical  
210 analyses that are accurate at the 95% confidence level to  $\pm X^{0.35}$ , where X is the concentration in wt. %.  
211 QXRD data is presented as a percentage of the rock volume (including porosity) so is consistent with  
212 previous studies (e.g. Fisher and Knipe, 1998, 2001).

213

#### 214 **Microstructure, mineralogy and petrophysical property results**

215 QXRD analysis indicates that the host sediments contain 54 to 73.4% quartz, 3 to 7.2% albite, 11.4 to 18.7%  
216 microcline, 1.4 to 4.4% mica, 1.4 to 17% kaolin and small amounts (<1%) of pyrite. The undeformed  
217 sandstones have a diagenetic history that is typical of Jurassic sandstones in the North Sea that have been  
218 buried to 2800 m. In particular, they have experienced the precipitation of early K-feldspar overgrowths  
219 and kaolin during shallow burial. Mechanical compaction was the main process for reducing porosity and

220 permeability during intermediate burial. The sandstones then experienced small amounts of quartz  
221 precipitation and grain contact quartz dissolution.

222 Examination of the structure of the samples in core suggested that most of fault rock samples are  
223 phyllosilicate-framework fault rocks (PFFR, Fisher & Knipe, 2001). Microstructural analysis confirms that  
224 PFFR are common (Fig. 9) but also indicates that protocataclasites, occasionally with a PFFR border (Fig.  
225 10) and to a minor extent cataclasites were also present. In general, many of the samples had 12 to 18%  
226 clay, which places them on the border between clean (<15% clay) and impure (>15% clay) sandstones. So  
227 the fault rocks that they contained tend to have characteristics of those expected generally formed from  
228 clean sandstones (i.e. domains with pore space that is free from clay) whilst other characteristics are typical  
229 of faults formed from impure sandstones (e.g. domains with macroporosity being filled by clay as well as  
230 having experienced enhanced grain-contact quartz dissolution); this makes a clear classification of the fault  
231 rocks difficult. It should be noted that PFFR's were originally defined as having flow properties that were  
232 controlled by presence of a continuous phyllosilicate-rich matrix between the framework grains (Knipe *et*  
233 *al.*, 1997). Later a generalization was made that such fault rocks tend to occur in sandstones containing 15-  
234 40% clay (Fisher and Knipe, 1998, 2001). However, the clay content of 15-40% should not be viewed as  
235 fixed values. Indeed, the discussion on clay mixing models presented below highlights how the sorting of  
236 the sand grains, which make up the framework of fault rocks, has a major impact on their petrophysical  
237 properties.

238 The ratio of the host rock and the fault rock absolute permeabilities is an important parameter that describes  
239 the retardation of fluid flow by faults (Yaxley, 1987). Figure 11 shows the data measured from the field  
240 and a range of data points from an in-house database from the same area that have the same stratigraphic  
241 range and burial depth. Both datasets were measured under ambient stress using distilled water as the  
242 permeant. The results demonstrate a permeability reduction of up to three orders of magnitude for the field  
243 data. The permeability reductions experienced implies that the fault rocks could have a significant impact  
244 on the single-phase flow especially when situated near to a production or injection well. The acquired data  
245 from the field fit well into global range, although the permeability reduction seems to be slightly less than  
246 in the global dataset. The reduction in permeability occurred as a result of a variety of processes including:  
247 faulting-induced grain fracturing, faulting-induced mixing of framework grains with phyllosilicate grains  
248 and enhanced grain contact quartz dissolution due to the presence of clays at grain contacts. It is apparent  
249 that there is no clear relationship between the fault rock type and the permeability reduction. However, the  
250 host rock permeabilities in the more impure sandstones are lower than in the clean sandstones, which is in  
251 line with previous work. There does not seem to be a correlation between the clay content of the protolith  
252 and the permeability reduction (Fig. 11) although dataset from the field itself is rather limited.

253 The brine permeability of all fault rocks showed a clear stress dependency (Fig. 9 and Fig. 10). In particular,  
254 the stress sensitivity of permeability increases as samples become less permeable (Figure 12). Fault rock  
255 samples with >0.1 mD permeability at ambient conditions tend experience permeability reductions of a  
256 factor of ~2 when confining pressure is increased to in situ conditions. On the other hand, lower  
257 permeability fault rocks often experience an order of magnitude reduction in permeability as confining  
258 pressure is increased to in situ conditions. The increased stress dependency of permeability with reduced  
259 permeability is consistent with permeability measurements made on other low permeability rocks such as  
260 tight gas sandstones (Thomas & Ward, 1972; Wei *et al.*, 1986; Kilmer *et al.*, 1987). Extrapolating the  
261 power-law relationship between stress and confining pressure to 70psi indicates that previous  
262 measurements made at ambient stress conditions are between 2 and 20 times higher (average difference is  
263 5 fold) than those made at high confining pressures. It should be emphasised that much of this stress  
264 sensitivity is likely to be caused by presence of grain-scale microfractures that formed during and/or  
265 following coring. The permeabilities of fault rock samples are therefore not likely to be as stress sensitive  
266 in the subsurface as in the laboratory, because microfractures will not be present in the subsurface and pores  
267 with low aspect ratios are not as stress sensitive unless an increase in stress results in brittle failure of the  
268 faults.

269 Fault rock permeabilities not only depend on the stress applied, but also on the fluid composition used  
270 during the experiments. The data shown in Figure 13 demonstrate that the permeabilities for a formation  
271 compatible brine are around 5 fold higher than for a deionized water, which has been used as the permeant  
272 for these type of measurements (Fisher & Knipe, 1998, 2001; Sperrevik *et al.*, 2002).

273 An important observation made during this work, incorporating a larger fault rock data set from different  
274 unpublished sources is that the effects of applying reservoir stress versus ambient stress and using brine  
275 versus deionized water cancel each other almost out and almost a 1:1 relationship seem to exist (Fig. 14).  
276 This implies that previously published fault rock property data (Fisher & Knipe, 1998, 2001; Sperrevik *et al.*,  
277 2002; Jolley *et al.*, 2007) can be still used with a certain confidence. This will be the subject of a future  
278 publication but it is important for the current study as it justifies using the legacy fault rock data along with  
279 the new measurement from the field to derive predictive functions for the fault rock permeability versus  
280 fault rock clay content for the reservoir scale faults.

281 It has been pointed out earlier that a sample bias exists, as some faults, particularly the ones with a higher  
282 clay content fault rock or with clay smear, could not be sampled, as the samples tend to break apart along  
283 the faults. So the sampled fault rocks mainly resemble the low to medium clay content fraction with some  
284 that show properties of phyllosilicate-framework fault rocks (Fig. 15). A relationship between the fault rock  
285 type and the fault rock permeability exists, despite the fact that differences in permeabilities of up to two

286 orders of magnitude exist for a similar fault rock clay content are measured (Fig. 15). This observation is  
287 consistent with earlier published datasets (Fisher & Knipe, 2001; Sperrevik *et al.*, 2002; Jolley *et al.*, 2007).

288

### 289 **Reservoir-scale fault property prediction**

290 To calculate the reservoir and small-scale (lineaments from seismic attribute analysis, see Fig. 4) fault  
291 properties a structural framework and a static geomodel has been established. The basis for the model is  
292 provided by 3D structural interpretation on a PreSDM dataset and a host rock Vclay model based on the  
293 Vclay logs from the four exploration wells, applying an appropriate depositional model. The fault rock  
294 clay content has been calculated varying the clay content of the host rock model according to the  
295 uncertainties from the petrophysical evaluations. Different fault zone clay predictors, such as SGR  
296 (Yielding, 2002) and ESGR (Freeman *et al.*, 2010) were assessed. The SGR at any point of the fault is  
297 given by a uniform average of the clay contents of the wall rocks that moved past this point (Yielding 2002).  
298 In contrast, the ESGR applies an additional weighting function to the averaging, which assumes that clays  
299 that are closer to the point of interest contribute more to the fault rocks (Freeman *et al.*, 2010). To link the  
300 fault rock permeability to the fault rock Vclay content; SGR/ESGR for reservoir scale faults; different  
301 predictive functions were applied. In addition the impact of potential clay smear on the production figures  
302 has been evaluated, together with changes in the relationship of fault rock thickness versus fault throw.  
303 Variations in fault throw can have a significant effect on the fault rock properties and reservoir/reservoir  
304 juxtaposition patterns in the field. Therefore an uncertainty on the throw of 20% has been incorporated.

305 The majority of the reservoir-scale faults fall into the PFFR domain, followed by clay smears and  
306 disaggregation zones/(proto)cataclastic fault rocks (Fig. 17). No significant difference in the distribution is  
307 apparent between the fault rock Vclay content when calculated using either SGR (Yielding, 2002) or ESGR  
308 (Freeman *et al.*, 2010), with a weighting factor of 1.5, as a fault rock Vclay prediction algorithm. A more  
309 detailed analysis of the Vclay distribution on the fault plane reveals that the ESGR algorithm predicts a  
310 more discrete distribution of Vclay, compared to the SGR algorithm (Fig. 17). The aim was to verify the  
311 influence of the application of the two different algorithms on the final dynamic simulation results.

312 The fault rock property data acquired during this study are limited in terms of their statistical value as only  
313 around 15 samples of small offset faults (<1 cm throw) were analysed and they do not represent the range  
314 of reservoir scale fault rocks (see Fig. 16). To have a statistically valid dataset the field data were combined  
315 with data from an in-house database, obtained from the same province, same stratigraphic interval and  
316 similar burial depth (Fig. 18). The measurements for the additional data were done under 70psi stress and  
317 with deionized water as reservoir fluid, which has discussed above are probably fine to use as the use of

318 distilled water appears to compensate for the impact on permeability of making the measurements at low  
 319 confining pressures. A cross-plot of fault rock permeability vs. clay content for this larger dataset from  
 320 analogue faults also has a very large amount of scatter as was the case for the measurements made during  
 321 this study.

322 Revil & Cathles (1999) demonstrate that the permeability of the sand/clay mixtures, which is essentially  
 323 what clay gouges represent, is controlled by the proportion of the host-rock sand and host-rock clay present,  
 324 the porosity and permeability of the sand end-member as well as the permeability of the shale end-member.  
 325 The porosity of the host-rock sand is controlled by grain sorting. These factors might explain the scatter of  
 326 the points in the  $V_{cl}$  versus permeability plot (Fig. 18). The objective was to represent the ranges between  
 327 fault rock  $V_{cl}$  content and fault rock permeability for the reservoir scale faults. A High-, Mid- and Low-  
 328 fault rock permeability predictive function has been established (Fig. 19a). The functions are based on a  
 329 model for the permeability of clay-sandstone mixtures ( $k_m$ ), presented by Revil *et al.* (2002).

330

$$331 \quad k_m = k_{sd}^{1 - \frac{V_{cl}}{\phi_{sd}}} \times k_{Cfs}^{V_{cl}/\phi_{sd}}, 0 \leq V_{cl} \leq \phi_{sd}$$

332

$$333 \quad k_m = k_{sh} V_{cl}^{3/2}, \phi_{sd} \leq V_{cl} \leq 1$$

334

335 where,  $\phi_{sd}$  and  $k_{sd}$  are the porosity and permeability of the clay-free sand,  $k_{sh}$  is the permeability of the  
 336 shale end-member and:

$$337 \quad k_{Cfs} = k_{sh} \phi_{sd}^{3/2}$$

338

339  $V_{cl}$  is the clay content of the fault rock, e. g. SGR or ESGR for the reservoir scale faults and  $k_{Cfs}$  is the  
 340 permeability of the clay-filled sand at the boundary between the clayey sands and sandy shales (Revil *et*  
 341 *al.*, 2002). The three functions were calculated by establishing three sand-clay mixing models, using the  
 342 parameters in Table 1. A good fit to the data for the three functions becomes apparent (Fig. 19a). The field  
 343 data, despite there are only few, fall clearly within the Mid- and Low-case scenario from Revil *et al.* (2002).

344 Comparing the Revil *et al.* (2002) High, Mid and Low fault rock permeability functions with algorithms  
 345 published previously by Sperrevik *et al.* (2002) and Jolley *et al.* (2007) for similar conditions (burial depth  
 346 <3000m), it becomes apparent that the latter predict a higher permeability of the fault rocks than indicated  
 347 by the field data (Fig. 19b).

348 The final input parameter into the reservoir simulator are TMs that are applied to the faces of grid blocks  
349 on either side of the fault plane to take into account the impact of faults on fluid flow. The TM calculation,  
350 as described by Manzocchi *et al.* (1999), requires information on the permeability of the undeformed  
351 reservoir in each grid block, the fault thickness and the fault permeability. The prediction of the fault rock  
352 thickness is one of the most uncertain parameters. There is a significant scatter in the data, but a 1:100  
353 relationship of fault thickness versus throw is commonly used. Freeman *et al.* (2008) suggest that a 1:66  
354 relationship is more appropriate for seismic-scale faults. Both relationships were incorporated into the  
355 calculation of the fault TMs.

356 An uncertainty also exists in the calculation of the Vclay content for the well logs and hence for the Vclay  
357 model as such. A 10% uncertainty has been estimated, based on petrophysical analysis, for the host rock  
358 Vclay content and fault rock property cases were calculated accordingly. In addition potential facies  
359 variations were taken into consideration in the uncertainty modelling.

360 Many properties are linked to the fault throw, such as the reservoir juxtaposition pattern, fault rock clay  
361 content prediction, the fault rock thickness and ultimately the TM, as the main input into the dynamic  
362 simulation. The fault throw is influenced by three main factors, the accuracy of the seismic migration, the  
363 quality and resolution of the seismic data and the structural interpretation. In this case, an uncertainty of the  
364 throw of 20% has been considered, based on the above mentioned parameters. A variation of the throw in  
365 the static geomodel alters the model geometry and sometimes it is difficult to carry this distorted geometry  
366 forward in the dynamic simulation. In order to keep the complexity at an acceptable level, it has been  
367 decided to calculate only one case for the throw variation, e.g. increase the throw by 20% (throw 120%).  
368 An increase in throw is expected to result in a more disconnected reservoir, which would decrease the  
369 recoverable volumes and demonstrates a potential “low case” scenario. The effective-cross fault  
370 transmissibility (ECFT, Freeman *et al.*, 2010) is used in Figure 20 to illustrate the effects of an increase in  
371 throw. The ECFT, which is a normalized cross fault transmissibility, is computed using the harmonic  
372 average of the permeabilities of the undeformed foot wall adjacent to the fault, the fault rock and the  
373 undeformed hanging wall across the fault. This is done for a specific width of host wall rock on each side  
374 of the fault and the fault rock thickness by the local displacement (Freeman *et al.*, 2010). The lower reservoir  
375 interval is the one that contributes most to the recoverable volumes. An increase in throw reduces the area  
376 where the lower reservoir is self-juxtaposed (Fig. 20a & b). The fact that more zones with elevated ECFT  
377 in the area where the lower reservoir in the footwall is juxtaposed against the upper reservoir in the  
378 hangingwall occur (compare Fig. 20a and Fig. 20b), does not counterbalance this effect. This becomes  
379 evident in the dynamic simulation.

380

381

### 382 **Small scale fault property prediction**

383 In addition to the seismic faults numerous small-scale faults, without a visible offset in seismic exist. These  
384 faults can be observed as lineaments on seismic attribute maps (Fig. 4). It has been considered to be  
385 important to include these faults into the dynamic simulation model. The faults were mapped as lineaments  
386 and vertical fault planes without an offset were constructed in the dynamic model. As no offset is associated  
387 with these faults, their TMs cannot be calculated in the same way as for faults with an offset. Therefore a  
388 range of single TMs for the entire small scale fault surfaces was calculated, applying a range of fault throw  
389 (1m, 5m, 10m, 20m) with the corresponding fault rock thicknesses using a thickness to throw relationship  
390 of 1:100. A single average permeability value of 950 mD has been taken for footwall and hangingwall cells,  
391 based on a range of core measurements in the reservoir sandstones. A bulk fault zone permeability has been  
392 calculated using the harmonic average from the measured fault rock permeabilities from the cores, using a  
393 30% salinity brine and applying a stress of 4000psi. The harmonic average was used as the permeability  
394 required is that measured perpendicular to the fault. It has been concluded from applying the different  
395 scenarios that bulk TMs of 0.001, 0.01 and 0.1 represent a realistic range for the small scale faults.

396 At this stage of the analysis it is important to bear in mind that no history matching data exist in the field,  
397 which would allow a calibration of the results. It is important at this point in time to figure out which  
398 parameters have the most significant impact on the resulting recoverable volumes. Once history matching  
399 data are available this provides a good basis for a more focused analysis of the key influencing parameters.

400 A summary of the cases that were incorporated into the dynamic simulation is given in Figure 21.

401

### 402 **Simulation modelling results**

403 The scenarios discussed above were, together with other geological variables, incorporated into a fully  
404 integrated, automated workflow for dynamic reservoir simulation and uncertainty modelling (200  
405 iterations). The main goal was to identify which one of the many parameters, apart from the fault properties,  
406 in the uncertainty model have the most impact on the recoverable volumes and the recovery efficiency. An  
407 additional objective was to verify the impact of the different fault property cases on the recoverable volume  
408 range. In order to ensure that the results are comparable, the producer/injector well pattern has not been  
409 changed during the uncertainty simulation.

410 In Figure 22 the impact of the several calculated scenarios on the recoverable volumes is highlighted. In  
411 case a TM = 1 is applied, the recoverable volumes are as if there were no faults present, e.g. normalized to

412 100%. If the minimum case of recoverable volumes is valid, e.g. if low permeable seismic scale faults  
413 combined with low permeable small scale faults are present, the recovery would be only 70% compared to  
414 a model without faults. The dynamic simulation reveals that the clay content versus permeability  
415 relationship, together with variations in fault throw, have the most significant impact on the recoverable  
416 volumes (Fig. 22). Slightly tighter faults are predicted when the ESGR is used as a mixing algorithm. The  
417 impact of a thickness to throw ratio of 1:66 instead of 1:100 leads to a decrease in fault transmissibility, but  
418 not to a significant amount. The presence of clay smear does not lead to significantly tighter faults and  
419 hence causes only a minimal reduction in recoverable volumes because continuous clay layers are not  
420 predicted in the host rock model. The functions suggested by Sperrevik *et al.* (2002) and Jolley *et al.* (2007)  
421 seem to predict less influence of the faults on the subsurface fluid flow for this particular case. The  
422 incorporation of small-scale faults whose throw cannot be mapped can decrease the recoverable volumes  
423 again by up to 10%, compared to the cases where only the larger scale faults are taken into consideration.  
424 Combining the observations made on core-scale, with seismic attribute analysis strongly suggests the need  
425 to incorporate the small-scale faults into the model. The dynamic simulation with several fault property  
426 scenarios shows that a reduction between 10% and 30% of the recoverable volumes, compared to a model  
427 without or completely open faults, is likely.

428 The impact of the faults on the recovery efficiency and cumulative production were assessed in the  
429 uncertainty modelling. Apart from the fault properties, other parameters such as the variation on top and  
430 base reservoir grids, residual oil and water saturation and reservoir porosity and permeability were  
431 incorporated into the analysis. The properties of the faults are among the most influential parameters for  
432 the oil recovery efficiency. Using fault specific TMs, generated applying the above discussed workflow,  
433 versus a distribution of single TM values reduces the uncertainty by around 40% for the recovery efficiency.  
434 This is a very important result as it clearly demonstrates the value of a detailed fault analysis compared to  
435 just using single global values.

436 For the cumulative production the fault properties are an important, but not the most influential parameter.  
437 Again, using a fault specific TM grid, based on the above described fault analysis workflow, compared to  
438 applying a range of single TM reduces the uncertainty by 50%.

439

## 440 **Discussion**

441 The seismic interpretation, which is a key element that provides the basis for a quality fault analysis and  
442 the translation of the interpretation into the static geomodel, has not been discussed in detail in this paper.  
443 The seismic data quality across the field is only fair, which implies that that the fault and horizon picking

444 is associated with uncertainties; the same is also true for the velocity model. The possibility to run fully  
445 integrated uncertainty models really helped to incorporate these different parameters and assess their  
446 impact. However, a verification of effects from different interpretation concepts is not possible within this  
447 workflow, but would be a subject for further analysis, once the field is in development and history  
448 matching data exist, which allow a better calibration of the outcomes.

449 Similar fault styles are observed on core and seismic scale (compare Figure 2 with Figure 8). The  
450 availability of numerous fault rock samples from core, together with high quality borehole images was a  
451 real benefit for the work. In the first instance, these data highlight the complexity of the faulting, also  
452 below seismic resolution. Secondly, the fault rock data provide the basis for the calibration of the  
453 reservoir-scale fault rock permeability prediction. As demonstrated, the results from the absolute  
454 permeability measurements on these samples under reservoir stress conditions, using a reservoir  
455 compatible fluid are very similar to absolute permeability measurements under ambient stresses but using  
456 deionized water as a permeant (Fig. 14). It shall be pointed out, that this observation does not imply that  
457 the efforts for conducting measurements under realistic subsurface conditions are not necessary in the  
458 future, but highlights the possibility to use previously acquired datasets with a certain confidence.

459 We find that the functions developed by Revil *et al.* (2002) provide an appropriate description for sand-  
460 clay mixtures (fault rocks) and their related absolute permeabilities. Revil & Cathles (1999) demonstrate  
461 that the permeabilities of these mixtures are not only a function of the clay content, as suggested by  
462 previous authors (Fisher & Knipe 1998; Fisher & Knipe 2001). Functions that correlate the fault rock clay  
463 content to the fault rock permeability suggested by Sperrevik *et al.* (2002) and Jolley *et al.* (2007) seem to  
464 predict a lower impact of the faults on the subsurface fluid flow in this specific case. This can be due to  
465 various factors including:

- 466 i. The functions suggested by Jolley *et al.*, (2007) and Sperrevik *et al.*, (2002), which were used in this  
467 paper for comparison, are derived from regression lines through a cloud of data with a significant  
468 scatter for a given depth of burial. This implies that the high- and low-side will not be fully  
469 represented.
- 470 ii. **The** measurement setup, e.g. permeability measurements with deionized water at ambient stress  
471 does not represent real subsurface conditions, e.g. reservoir compatible brine at subsurface stress.
- 472 iii. The data used by Jolley *et al.* (2007) and Sperrevik *et al.* (2002) are not from the field, so the use of  
473 specific field data should provide more accurate ranges.
- 474 iv. The sand-clay mixing model proposed by Revil & Cathles (1999) appears to be a proper  
475 representation of the parameters that lead to the development of fault rocks and their properties..

476 It has been pointed out already that the work described in this paper lacks the calibration of the fault  
477 analysis results by history matching data or even long term well tests. Once the field is under  
478 development and production data exist, the exercise will have to be repeated and it is expected that the  
479 uncertainties can be significantly reduced. In any case, the current study provides a good basis for future  
480 work.

481

## 482 **Conclusions**

483 A better understanding of the fault properties by incorporating geologically sensible parameters played an  
484 important role in the uncertainty assessment for the field development planning. In this context the  
485 incorporation of fault rock measurements from field data, together with application of the algorithms from  
486 Revil *et al.* (2002) for the fault rock clay content prediction increased significantly the credibility of the  
487 analysis results. The fault properties are among the most critical and influential parameters especially for  
488 the recovery efficiency, but also for the cumulative production. It can be demonstrated that using a fault  
489 specific transmissibility multiplier grid versus a distribution of single, global transmissibility multiplier  
490 values significantly reduces the uncertainties for the recovery efficiency and cumulative recovery.

491

## 492 **Acknowledgements**

493 The authors thank Wintershall Norge AS, Capricorn Norge AS, Bayerngas Norge AS, DEA Norge AS,  
494 Repsol Norge As, Edison Norge AS and Explora Petroleum AS, for the permission to publish this paper.  
495 We also thank Eriksfiord and the CiPEG Leeds for the permission to present data generated by them for  
496 this study.

497

## 498 **References**

499 Brindley, G.W. (1984) Quantitative X-ray analysis of clays. Pp. 411-438 in: *Crystal Structures of Clay*  
500 *Minerals and their X-ray Identification* (G.W. Brindley & G. Brown, editors). Mineralogical Society,  
501 London.

502 Fisher, Q. J. & Knipe, R. J. 1998. Fault sealing processes in siliciclastic sediments. *In*: G. Jones, Q. Fisher  
503 and R. J. Knipe (eds) *Faulting and Fault Sealing in Hydrocarbon Reservoirs*. *Geological Society, London,*  
504 *Special Publication*, **14**, 117-134.

505 Fisher, Q. J. & Knipe, R. J. 2001. The permeability of faults within siliciclastic petroleum reservoirs of  
506 the North Sea and Norwegian Continental Shelf. *Marine and Petroleum Geology*, **18**, 1063-1081.

507 Fisher, Q.J. & Jolley, S.J. 2007. Treatment of faults in production simulation models. *In: Jolley, S. J.,*  
508 *Barr, D., Walsh, J. J. & Knipe, R. J. (eds) Structurally Complex Reservoirs. Geological Society, London,*  
509 *Special Publications, 292, 219-233.*

510 Freeman, S.R., Harris, S.D. & Knipe, R.J. 2008. Fault seal mapping – incorporating geometric and  
511 property uncertainty. *In: Robinson, A., Griffiths, P., Price, S., Hegre, J. & Muggeridge, A. (eds) The*  
512 *Future of Geological Modelling in Hydrocarbon Development. The Geological Society, London, Special*  
513 *Publications, 309, 5-38.*

514 Freeman, S.R., Harris, S.D. & Knipe R.J. 2010. Cross-fault sealing, baffling and fluid flow in 3D  
515 geological models: tools for analysis, visualization and interpretation. *Geological Society, London,*  
516 *Special Publications, 347, 257-282.*

517 Hardy, R. & Tucker, M.E. 1988. X-ray diffraction. *In: Tucker, M. E. (eds) Techniques in Sedimentology.*  
518 *Blackwell, Oxford, 191-228.*

519 Hillier, S. 1999. Use of an Air Brush to Spray Dry Samples for X-Ray Powder Diffraction. *Clay*  
520 *Minerals, 34, 127-135.*

521 Hillier, S. 2000. Accurate quantitative analysis of clay and other minerals in sandstones by XRD:  
522 comparison of a Rietveld and a reference intensity ratio (RIR) method and the importance of sample  
523 preparation. *Clay Minerals, 35, 291-302.*

524 Jolley, S.J., Dijk, H., Lamens, J.H., Fisher, Q.J., Manzocchi, T., Eikmans, H. & Huang, Y. 2007. Faulting  
525 and fault sealing in production simulation models: Brent Province, northern North Sea. *Petroleum*  
526 *Geoscience, 13, 321-340.*

527 Kilmer, N.H., Morrow, N.R., and Pitman, J.K. 1987. Pressure sensitivity of low permeability sandstones.  
528 *Journal of Petroleum Science and Engineering, 1, 65-81.*

529 Knipe, R. J., Fisher, Q. J., Jones, G. , Clennell, M. R., Farmer, A. B., Kidd, B., McAllister, E., Porter, J. R.  
530 & White, E. A. 1997. Fault seal analysis, successful methodologies, application and future directions. *In:*  
531 *Møller-Pederson, P. & Koestler, A. G. (eds) Hydrocarbon Seals - Importance for Exploration and*  
532 *Production. Norwegian Petroleum Society (NPF), Special Publication, 7, 15-37.*

533 Lever A., and Dawe, R.A. 1987. Clay migration and entrapment in synthetic porous media. *Marine*  
534 *and Petroleum Geology, 4, 112-118.*

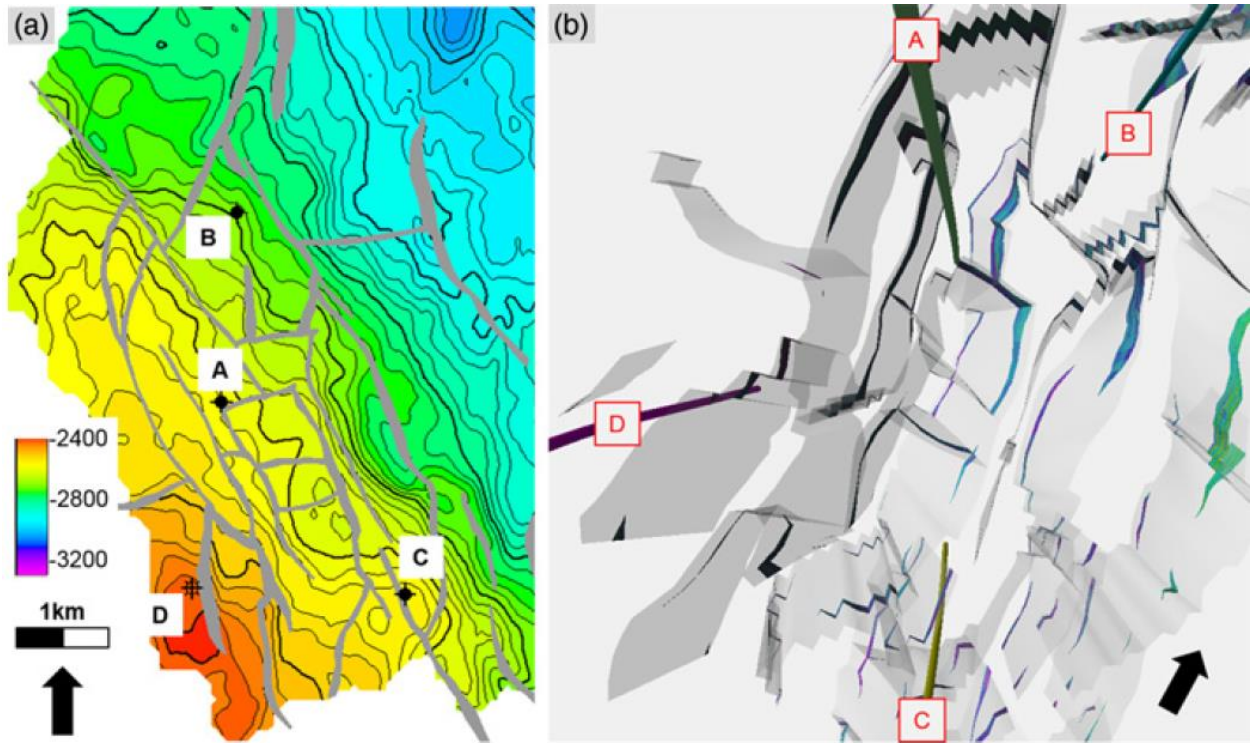
535 Manzocchi, T., Walsh, J.J., Nell, P. & Yielding, G. 1999. Fault Transmissibility Multipliers for flow  
536 simulation models. *Petroleum Geoscience, 5, 53–63.*

- 537 Revil, A. & Cathles L.M. 1999. Permeability of shaly sands. *Water Resources Research*, **35**, 651-662.
- 538 Revil, A.C., Grauls, D. & Brevart, O. 2002. Mechanical compaction of sand/clay mixtures, *Journal of*  
539 *Geophysical Research*, **107**, (B11), 2293.
- 540 Sperrevik, S., Gillespie, P.A., Fisher, Q.J., Halvorsen, T. & Knipe, R.J. 2002. Emperical Estimation of  
541 Fault Rock Properties. In : Koestler, A. G. & Hunsdale, R. (eds) Hydrocarbon Seals Quantification.  
542 *Norwegian Petroleum Society (NPF), Special Publication*, **11**, 109-125.
- 543 Thomas, R.W. & Ward, D.C. 1972. Effect of Overburden Pressure and Water Saturation on Gas  
544 Permeability of Tight Sandstone Cores, *JPT*, 120.
- 545 Wei, K.K., Morrow, N.R. & Brower, K.R. 1986. Effect of Fluid, Confining Pressure, and Temperature on  
546 Absolute Permeabilities of Low-Permeability Sandstones, *Society of Petroleum Engineers, Formation*  
547 *Evaluation*, 413.
- 548 Yaxley, L.M., 1987. Effect of a partially communicating fault on transient pressure behaviour. *Society of*  
549 *Petroleum Engineers, Formation Evaluation*, 590–598.
- 550 Yielding, G. 2002. Shale gouge ratio – calibration by geohistory. In : Koestler, A. G. & Hunsdale, R.  
551 (eds) Hydrocarbon Seals Quantification. *Norwegian Petroleum Society (NPF), Special Publication*, **11**, 1-  
552 15.

553

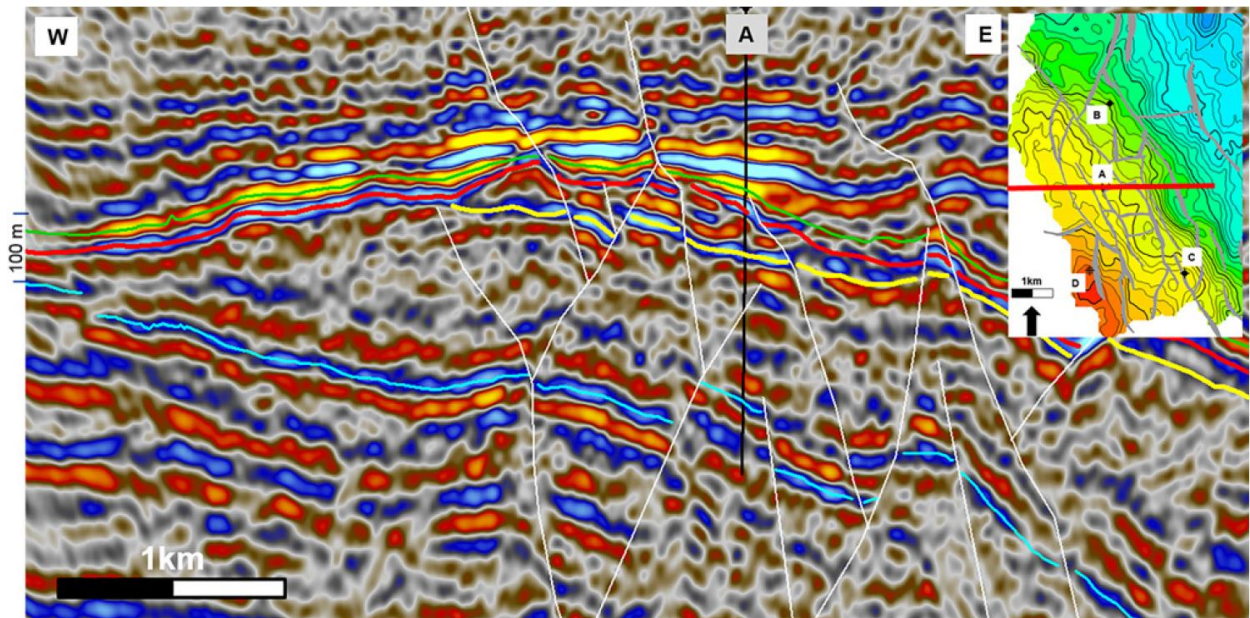
554

555 **Figure captions**



556

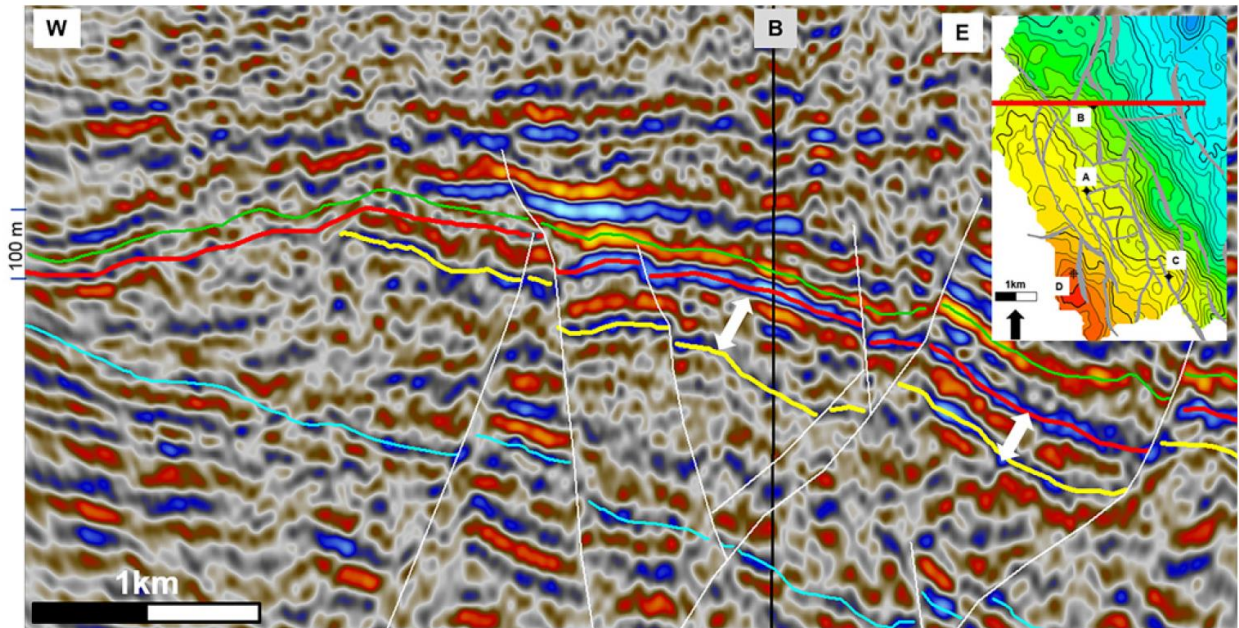
557 **Fig. 1** (a) Top reservoir depth map with the four exploration/appraisal wells (A-D) and the fault  
 558 polygons (b) 3D fault model from the static geological model (view from above), colored areas  
 559 (SGR) highlight reservoir/reservoir juxtaposition.



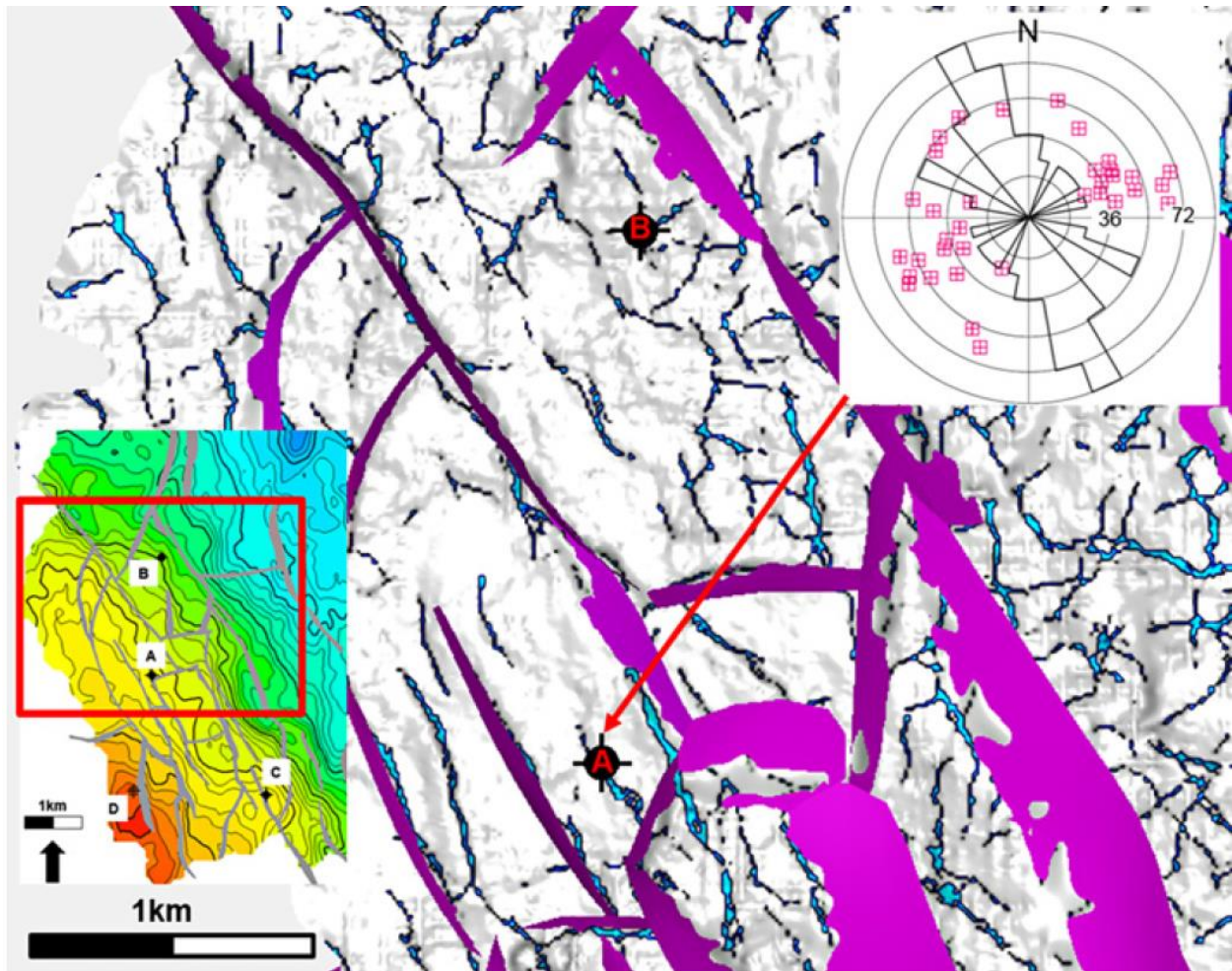
560

561 **Fig. 2.** Depth seismic section across the field, highlighting the structural complexity at reservoir  
 562 level. Note that most faults predate the unconformity (red horizon), but some also seem to have

563 younger movements. Green horizon = Base Cretaceous Unconformity, red horizon = near top  
564 reservoir and unconformity, yellow horizon = base reservoir, blue horizon = Top Brent Gp.

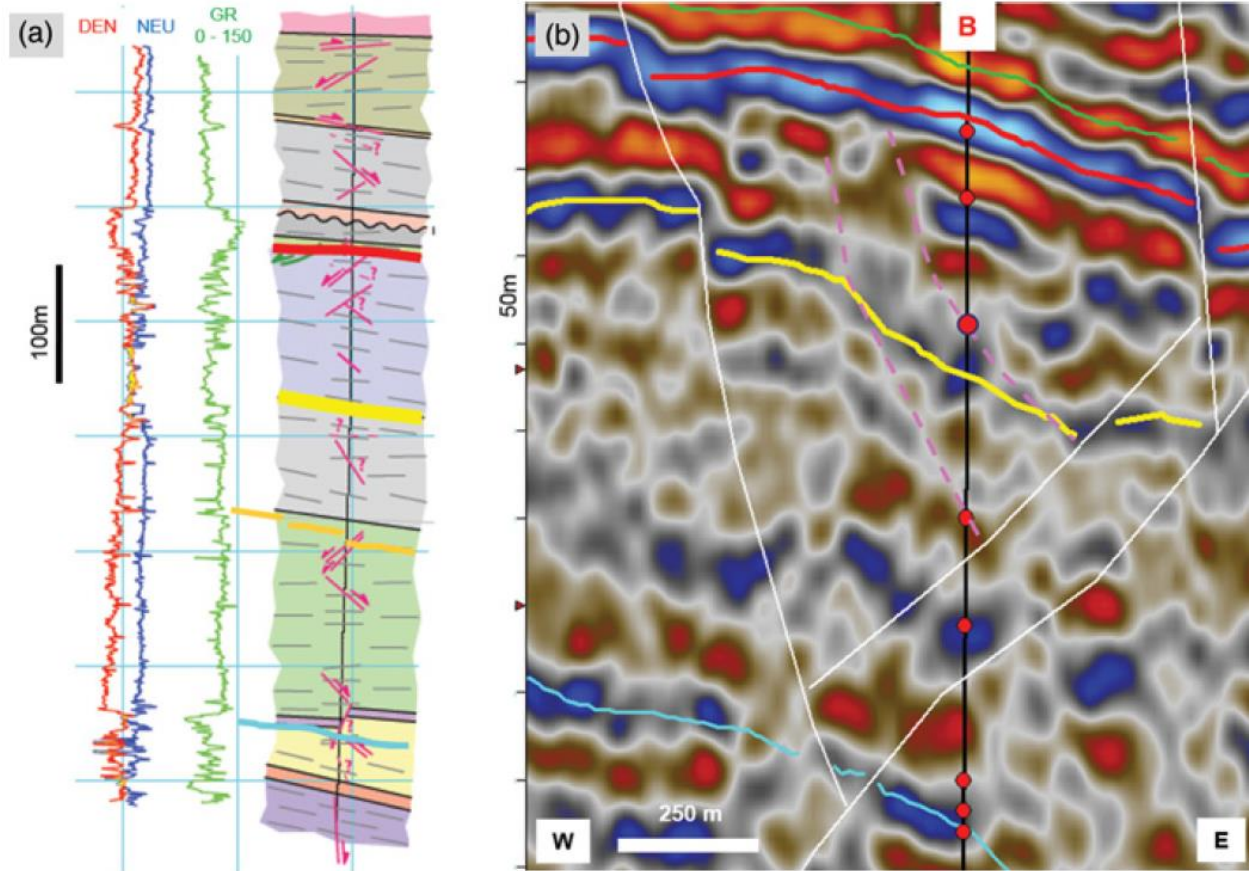


565  
566 **Fig. 3.** Depth seismic section across the field, highlighting the structural complexity at reservoir  
567 level. Note that most faults predate the unconformity (red horizon), but some also seem to have  
568 younger movements. Note the thickening across the faults (white arrows), indicating syntectonic  
569 deposition. Occasionally a dip refraction of the faults in the more shale rich lithologies between  
570 the base reservoir and top Brent Gp is visible. Green horizon = Base Cretaceous Unconformity,  
571 red horizon = near top reservoir and unconformity, yellow horizon = base reservoir, blue horizon  
572 = Top Brent Gp.



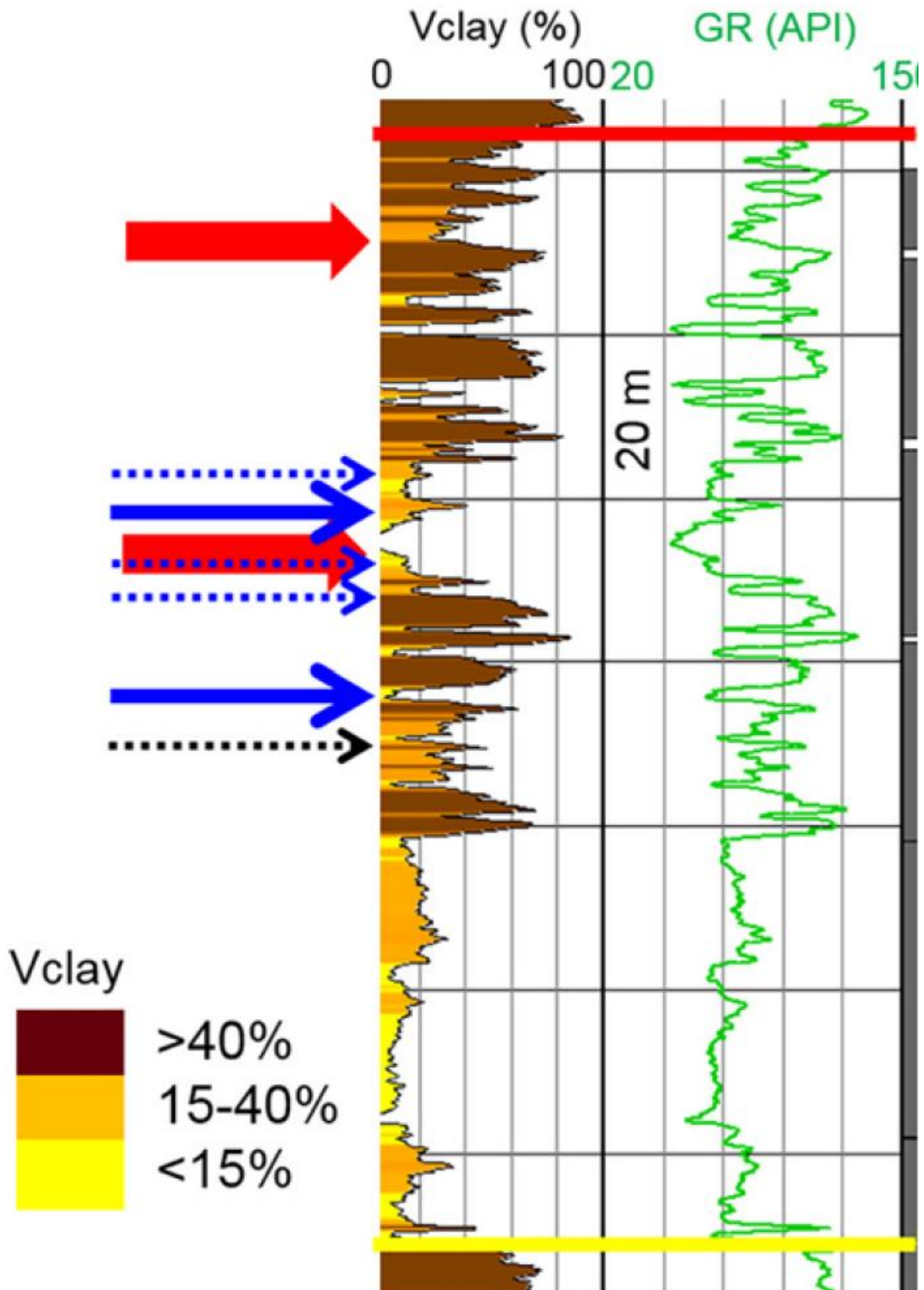
573

574 **Fig. 4.** Seismic attribute (Ant Tracking) map near the base reservoir, showing the main fault  
 575 planes that were interpreted on the seismic sections (coloured planes) and faults below seismic  
 576 resolution and without visible offset (blue lineaments). The strike histogram (SCHMIDT, Upper,  
 577 poles to planes) highlights the orientation of small scale faults identified from borehole image  
 578 analysis in well A. Note the good correlation with the lineament on the attribute map.

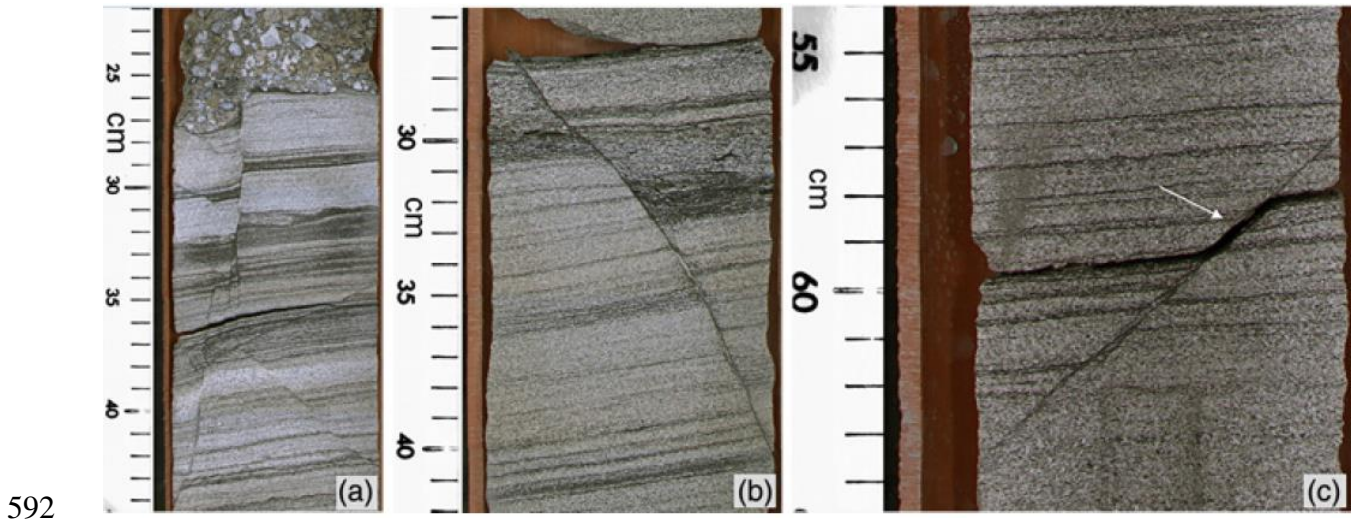


579

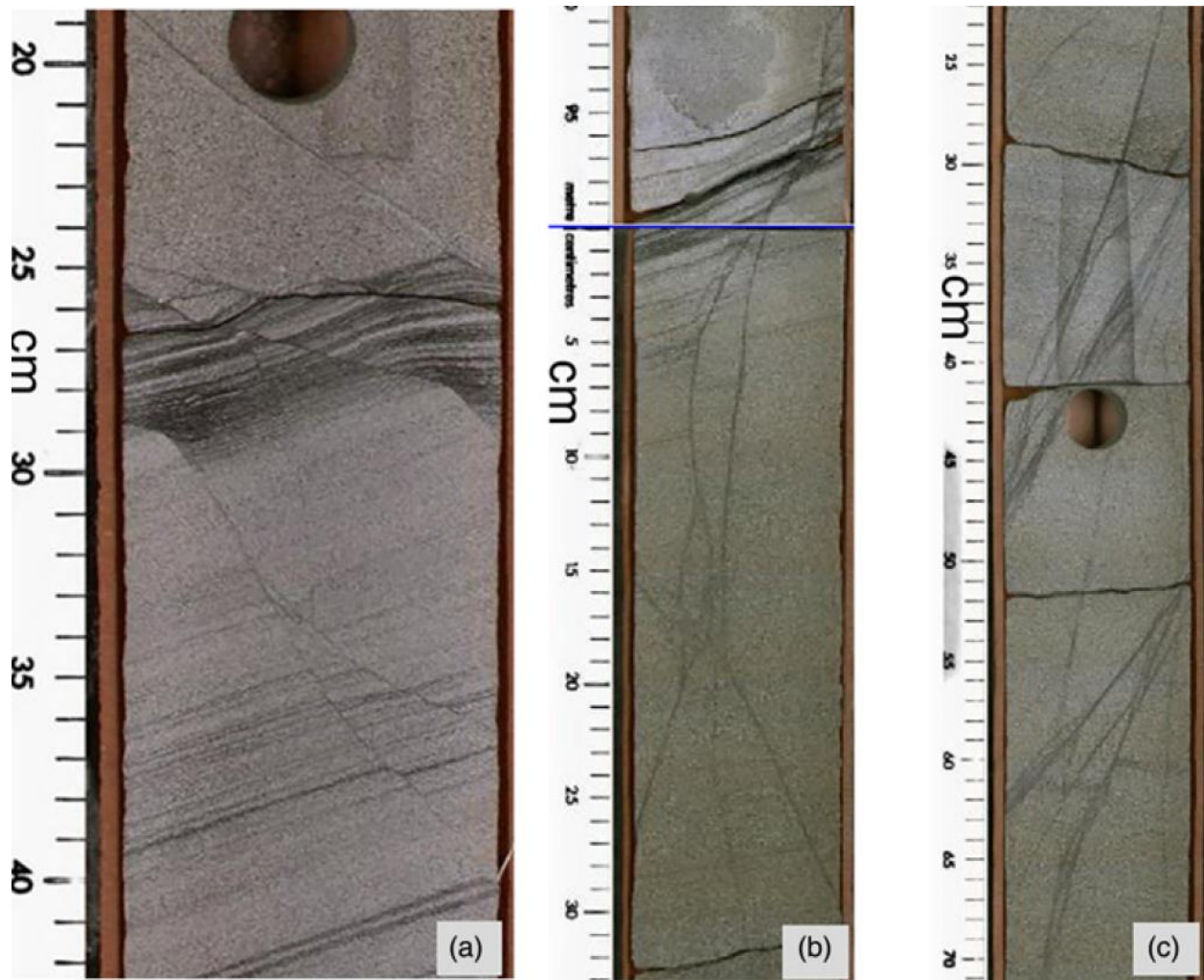
580 **Fig. 5.** (a) Schematic section through well B highlighting the main lithological units and the  
 581 faults (magenta) identified on borehole image logs. The colour coding for the horizons is  
 582 identical to the ones in (b). Near top reservoir = red line, base reservoir = yellow line, blue line =  
 583 top Brent Gp. (b) seismic cross section through well B with the top (red) and base (yellow) of the  
 584 main reservoir, seismic scale faults (white), sub-seismic scale faults (magenta), red dots highlight  
 585 faults identified on borehole image logs.



587 **Fig. 6.** Reservoir section from well B with Vclay and GR log. Bold red arrows = fault zones  
588 identified on image log. Solid blue arrows = fault rock samples displayed in Fig. 10 & 11.  
589 Stippled blue arrows = additional sampled and analyzed fault rocks. Stippled black arrow =  
590 sample in Figure 7c. Red line = top reservoir, yellow line = base reservoir. The grey section on  
591 the right side of the log represents the cored intervals.

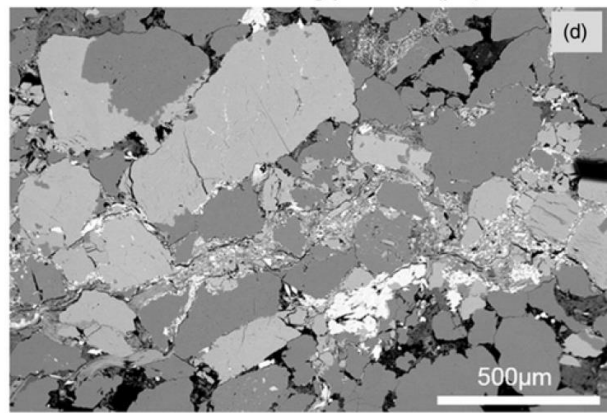
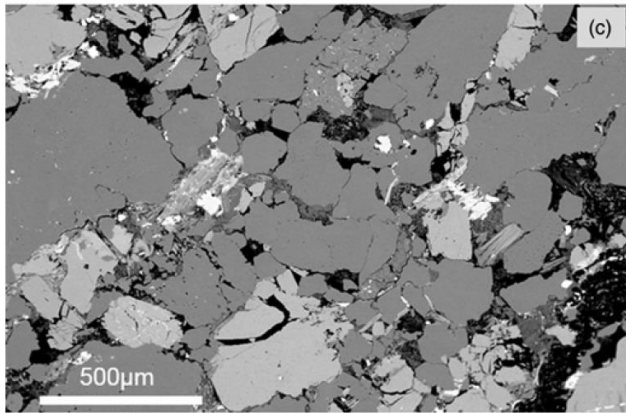
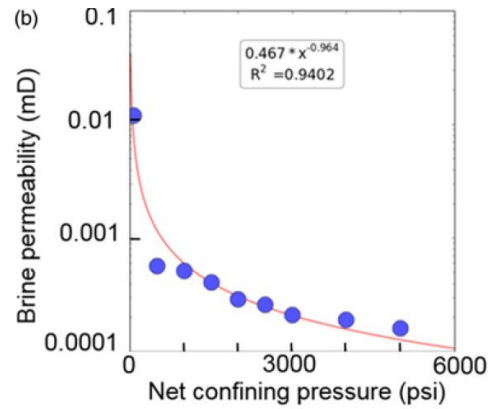


592  
593 **Fig. 7.** Cored small scale faults (a) Multiple normal faults. (b) Single normal fault with cm-offset  
594 of a clay-rich layer. The dark colored fault rock is enriched with phyllosilicates. (c) Normal fault  
595 with a cm-offset of a shale layer, developing a clay smear (white arrow); see also Figure 6 for  
596 location.



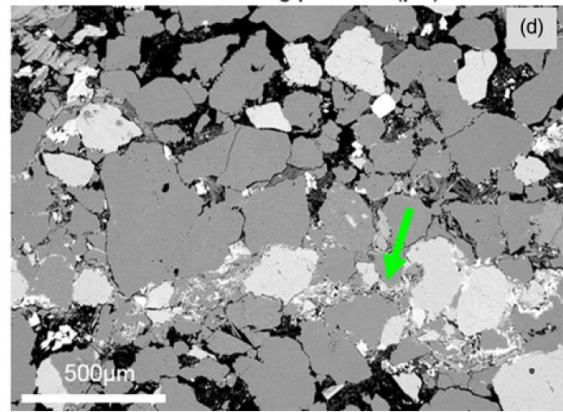
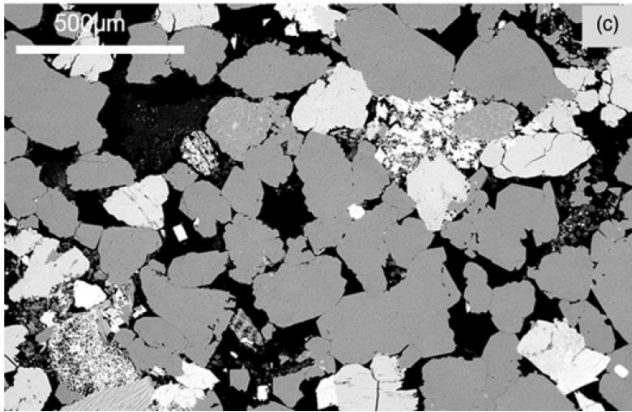
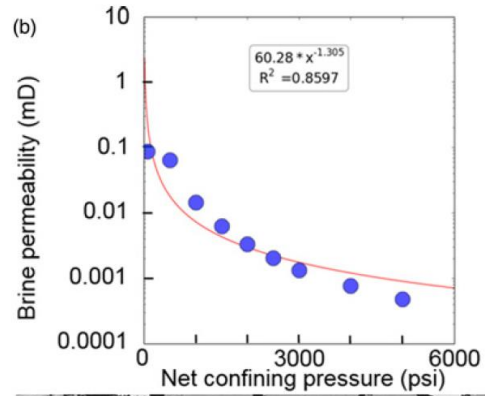
597

598 **Fig. 8.** Cored small scale faults and deformation bands (a) Small scale normal faults with cm-  
599 offset. Note the influence of the mechanical stratigraphy on the dip-angle of the fault plane. (b)  
600 Normal faulting in a clay-rich layer and deformation bands without visible offset in a clean  
601 sandstone package. (c) Deformation bands in a clean sandstone section. The dark color is due to  
602 trapped oil, which cannot escape due to the reduced porosity.



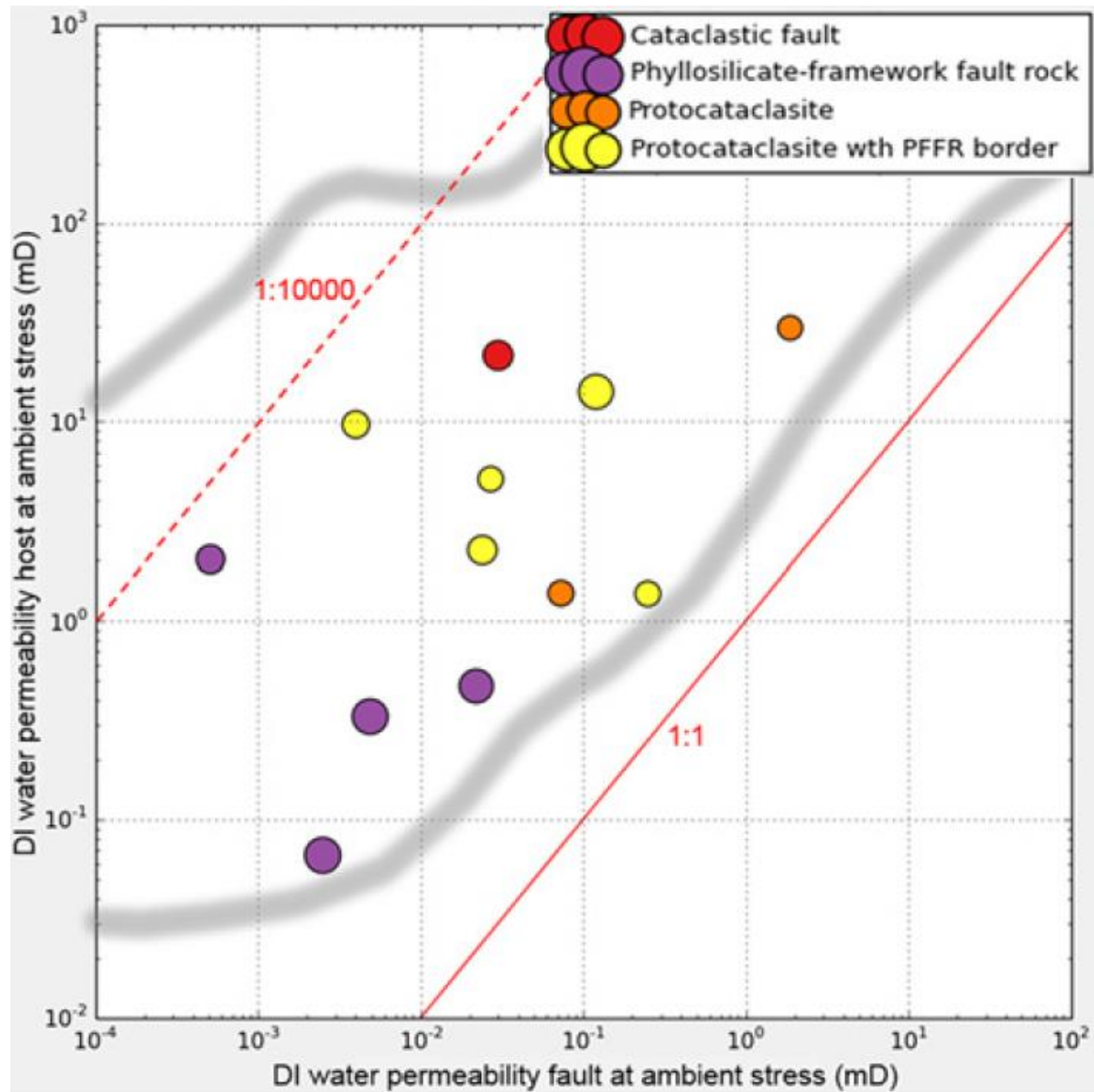
603

604 **Fig. 9.** Phyllosilicate framework fault rock (PFFR) in an impure sandstone. The offset of the  
605 fault is not visible. (a) core sample with a white arrow showing the position from where the  
606 sample for laboratory analysis was taken. (b) Results from absolute gas and brine permeability  
607 measurements from the host and fault-rock under different stresses. Note the stress-related  
608 permeability reduction. (c) BSEM image from host rock (d) BSEM image from fault rock.



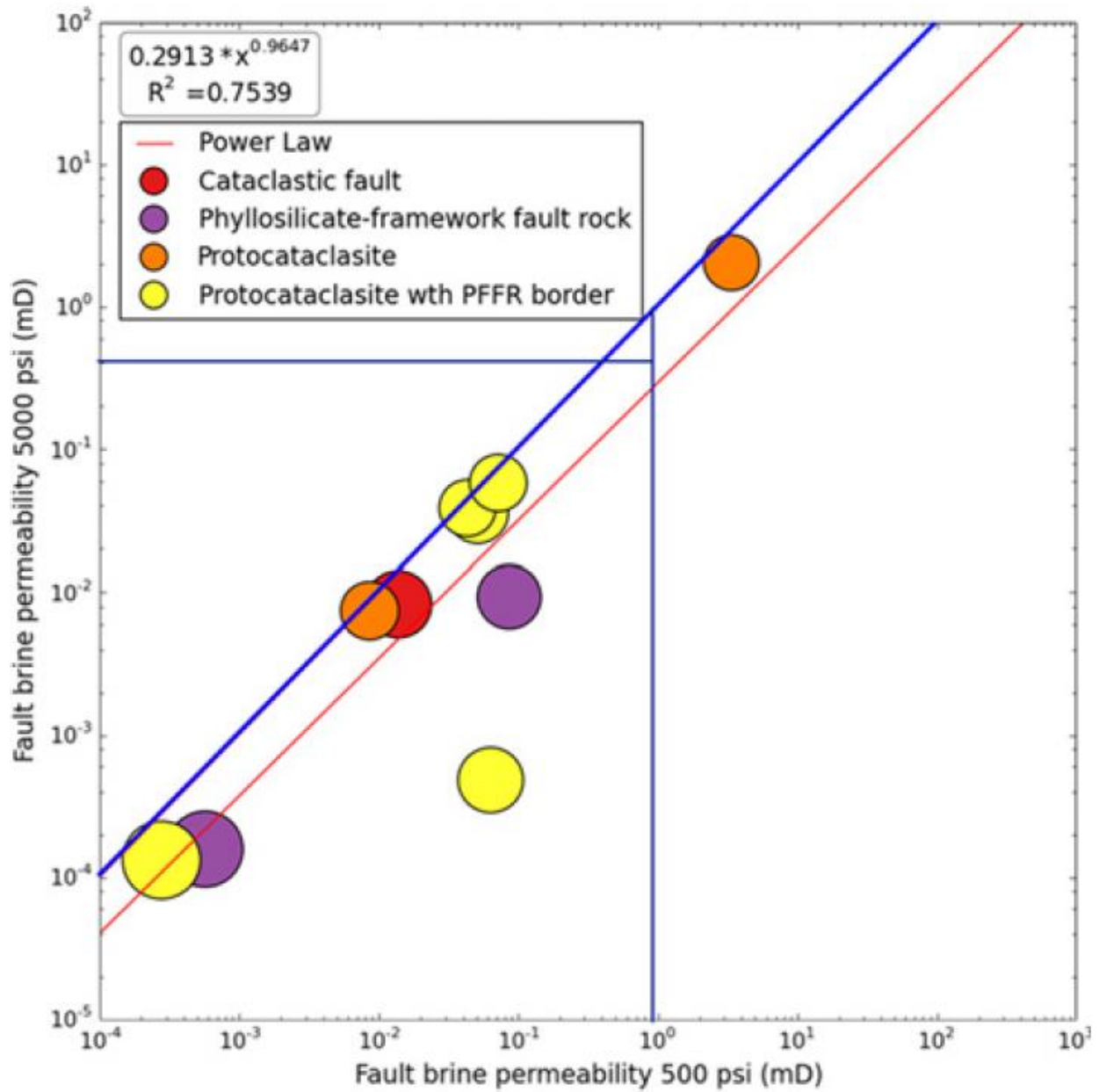
609

610 **Fig. 10.** Protocataclasite with PFFR border in a clean sandstone. The offset of the fault is not  
 611 visible (a) core sample with a white arrow showing the position from where the sample for  
 612 laboratory analysis was taken. (b) Results from absolute gas and brine permeability  
 613 measurements from the host and fault-rock under different stresses. Note the stress-related  
 614 permeability reduction. (c) BSEM image from host rock (d) BSEM image from fault rock; note  
 615 the PFFR border ( green arrow).



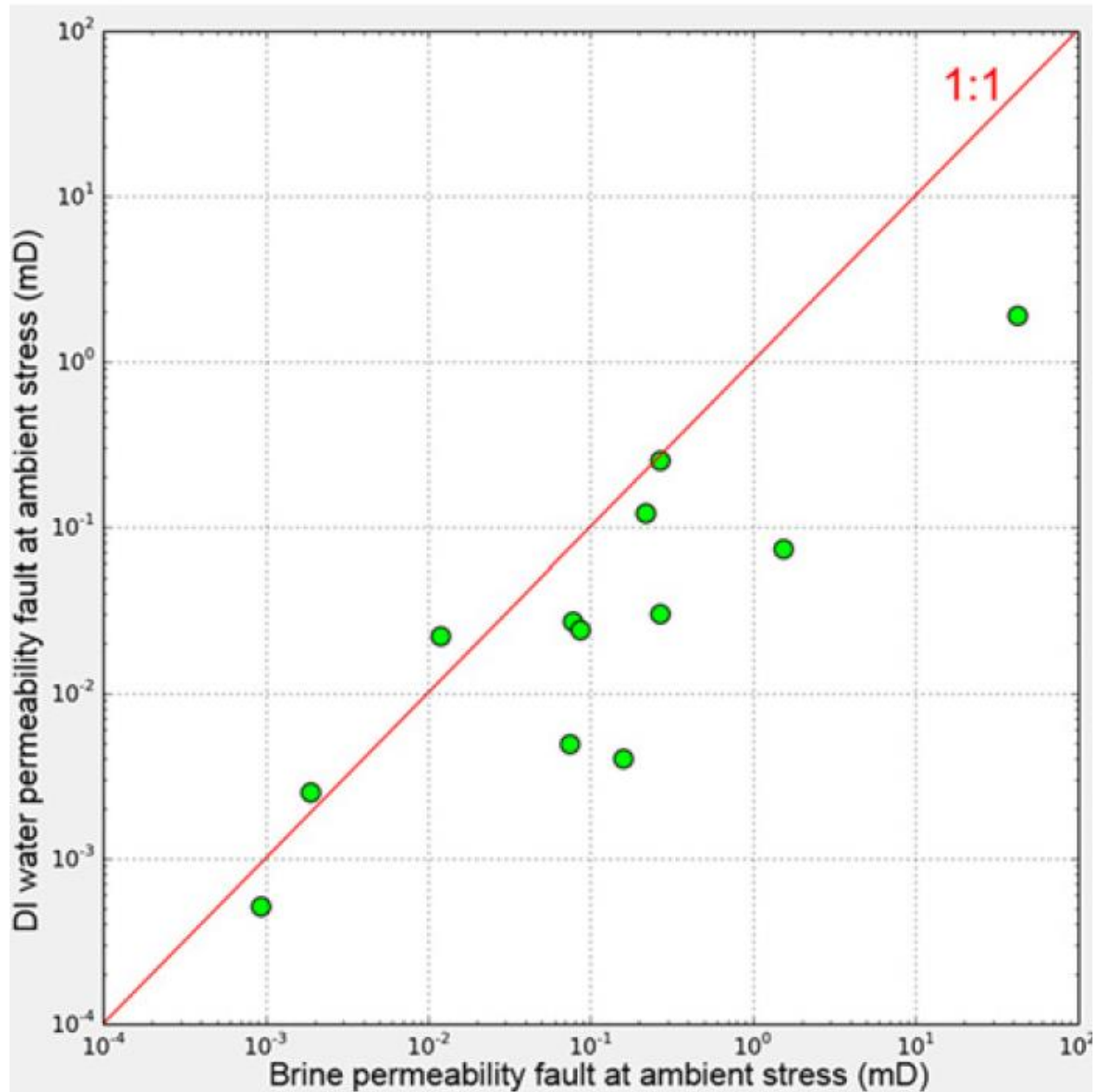
616

617 **Fig. 11.** Host rock versus fault rock absolute permeability measured under ambient stress and  
 618 with deionized water as reservoir fluid. The dots represent the field data. The grey outlines  
 619 represent the ranges of data from an in-house database. The point size correlates with the V<sub>clay</sub>  
 620 content of the fault rocks.



621

622 **Fig. 12.** Fault rock brine permeabilities from the field data under 500psi versus 5000psi. The  
 623 point size correlates to the fault rock Vclay content. Blue line = 1:1 relation, red line = power law  
 624 regression.

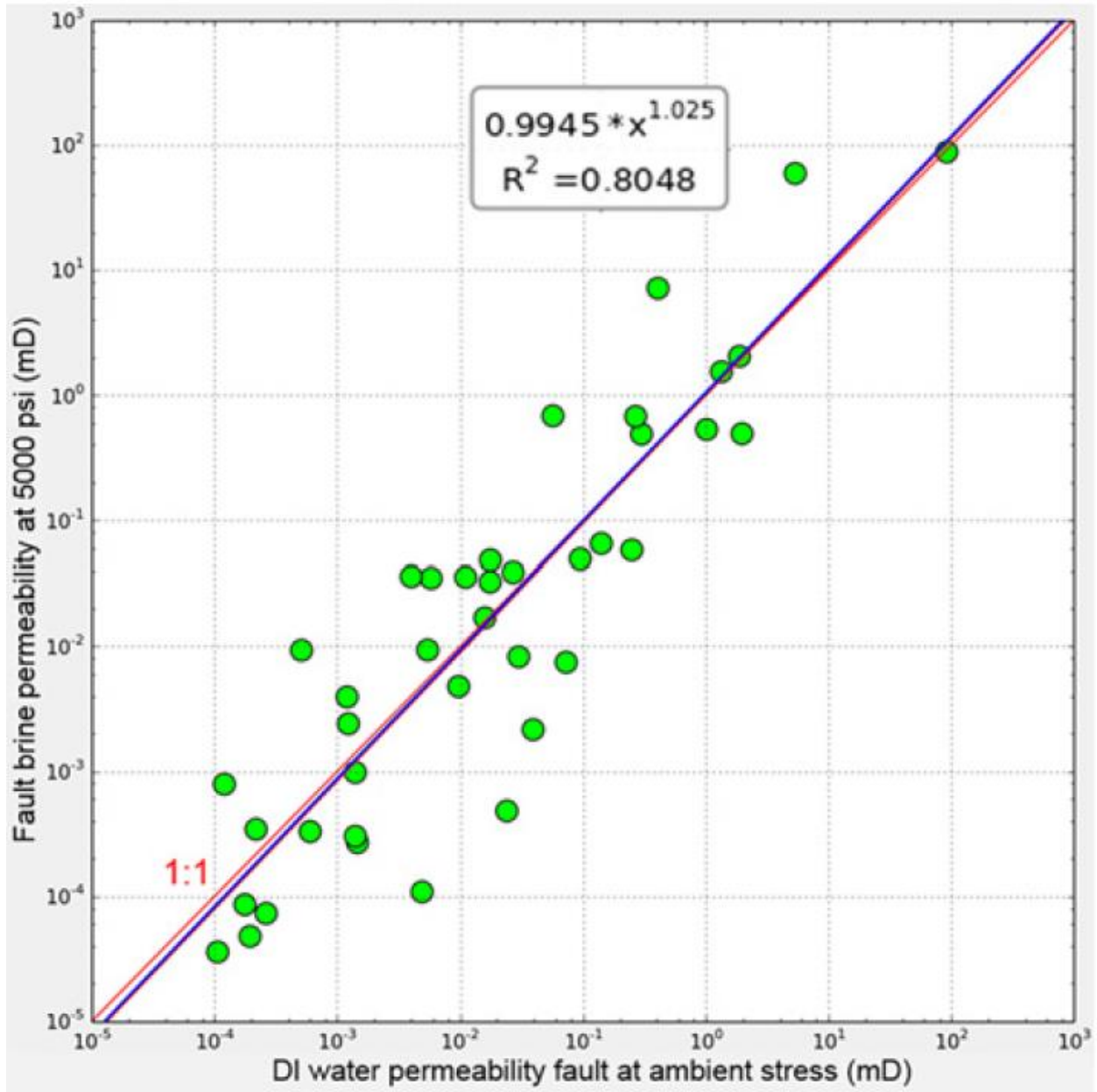


625

626

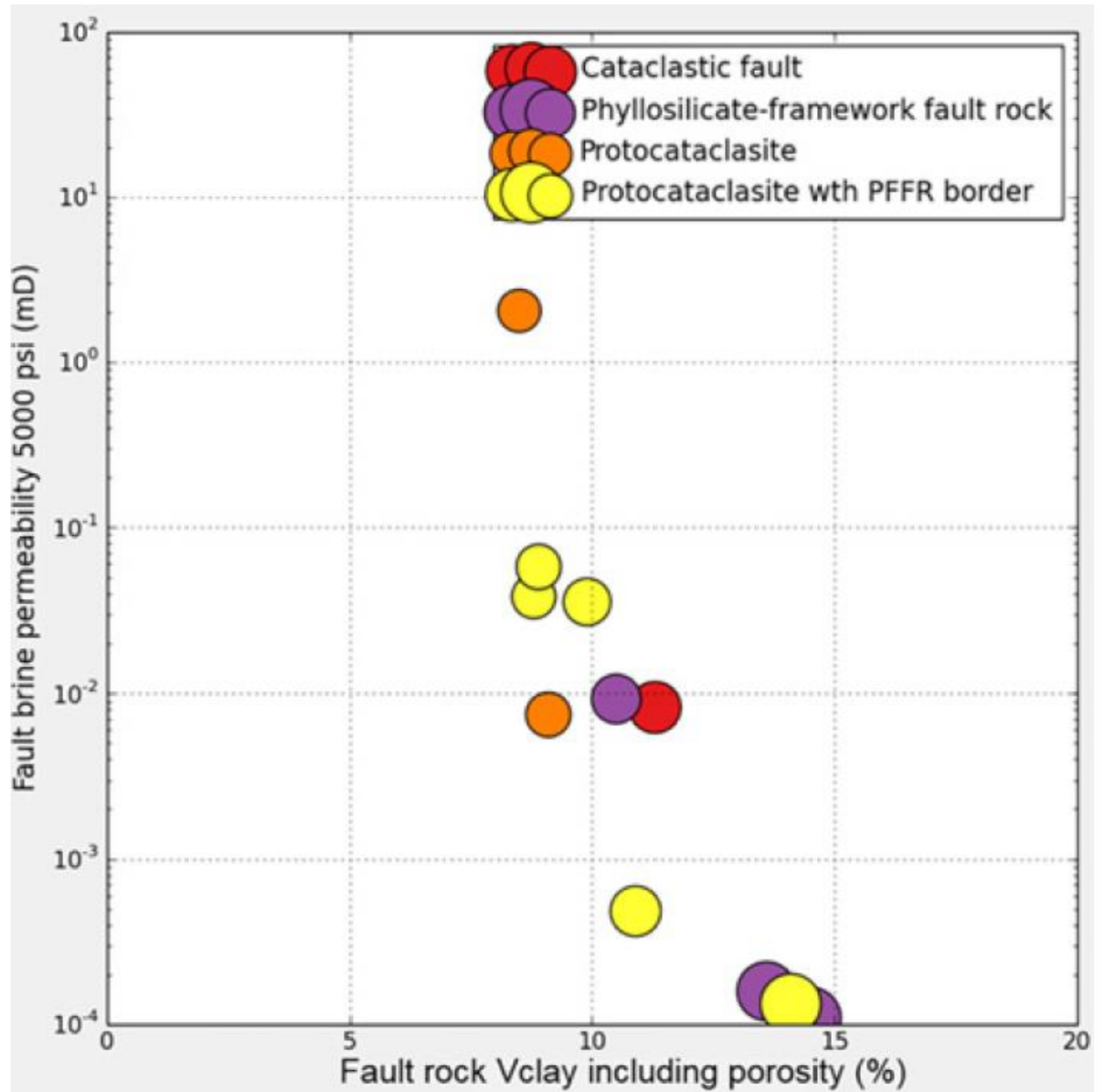
627

**Fig. 13.** Fault rock permeabilities from field data measured under ambient stress using a 30% salinity brine and deionized water as a reservoir fluid.



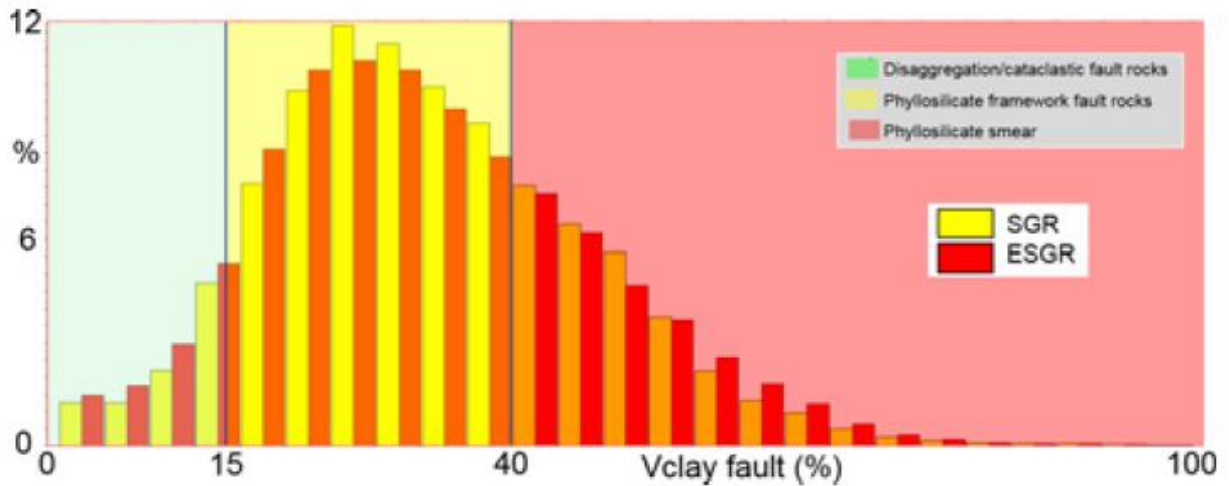
628

629 **Fig. 14.** Fault rock absolute permeabilities from a larger dataset measured under 5000psi stress  
 630 with formation compatible brine versus data measured at ambient stress and deionized water as  
 631 reservoir fluid. These fault rocks are similar to those analysed during the current study. The  
 632 observation that the regression (blue) is almost the same as the 1:1 relationship (red) between the  
 633 two measurement techniques suggests that it is reasonably safe to use the data collected at low  
 634 stress with distilled water as an analogue for measurements conducted at in situ stresses using  
 635 formation compatible brine.

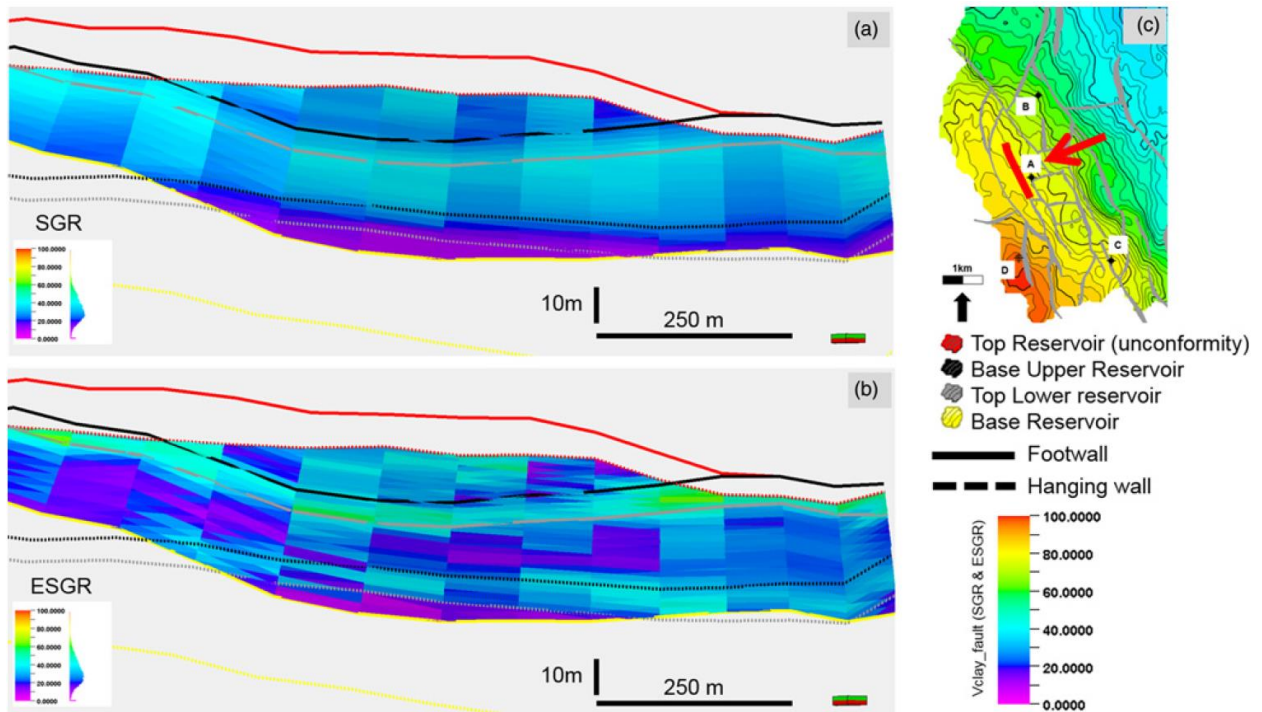


636

637 **Fig. 15.** Fault rock brine permeability under 5000psi stress plotted against the fault rock clay  
 638 content.

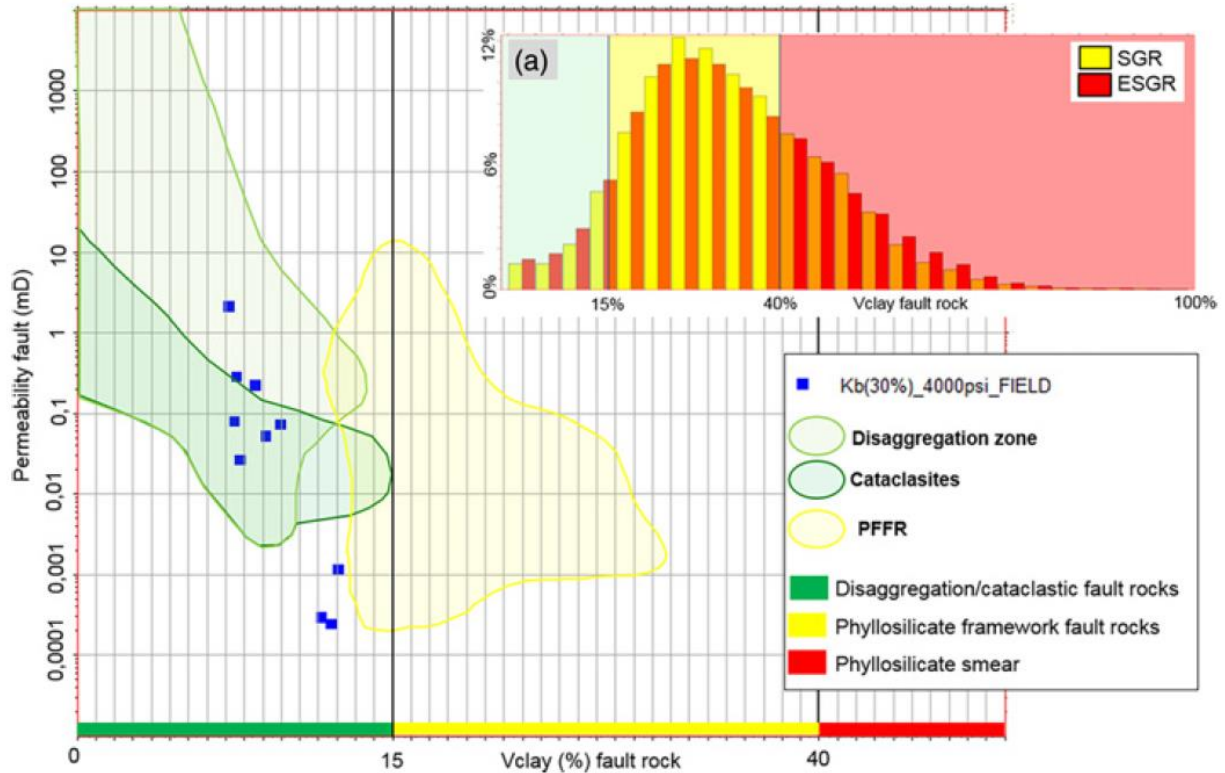


639  
 640 **Fig. 16.** Histogram plot of fault rock Vclay content for the reservoir scale faults based on a base  
 641 case Vclay geomodel and a base case fault throw. The difference applying the SGR (Yielding,  
 642 2002) and ESGR (Freeman *et al.*, 2010) algorithm as a fault rock Vclay predictor is shown. The  
 643 ESGR is for a hangingwall and footwall combination with a weighting factor of 0.15.

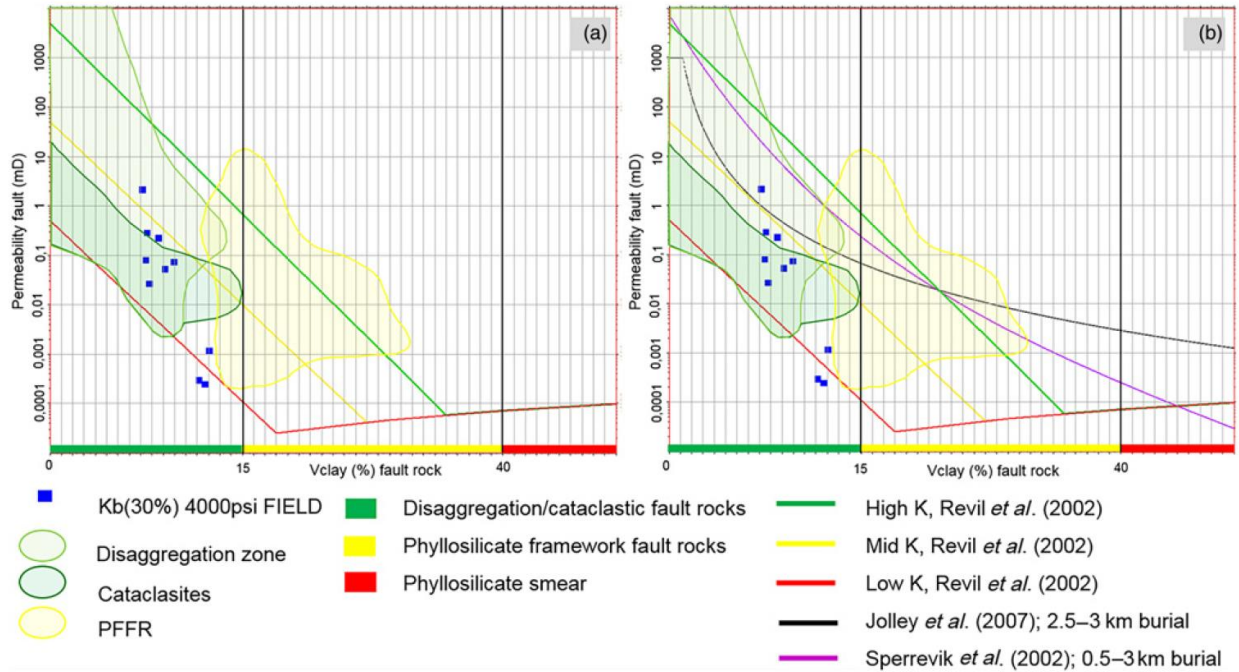


644  
 645 **Fig. 17.** Calculated fault rock Vclay content applying two different fault rock Vclay prediction  
 646 algorithms (a) SGR (b) ESGR. (c) Near top reservoir map with seismic scale faults. The area  
 647 colour coded with fault properties on 'a' and 'b' corresponds to the reservoir-reservoir self-

648 juxtaposition. Note that the reservoir is divided further into an upper and lower interval with a  
 649 more silty layer in-between (see also Fig. 6); between the black and grey horizon. The view is  
 650 towards the SW onto the fault plane.

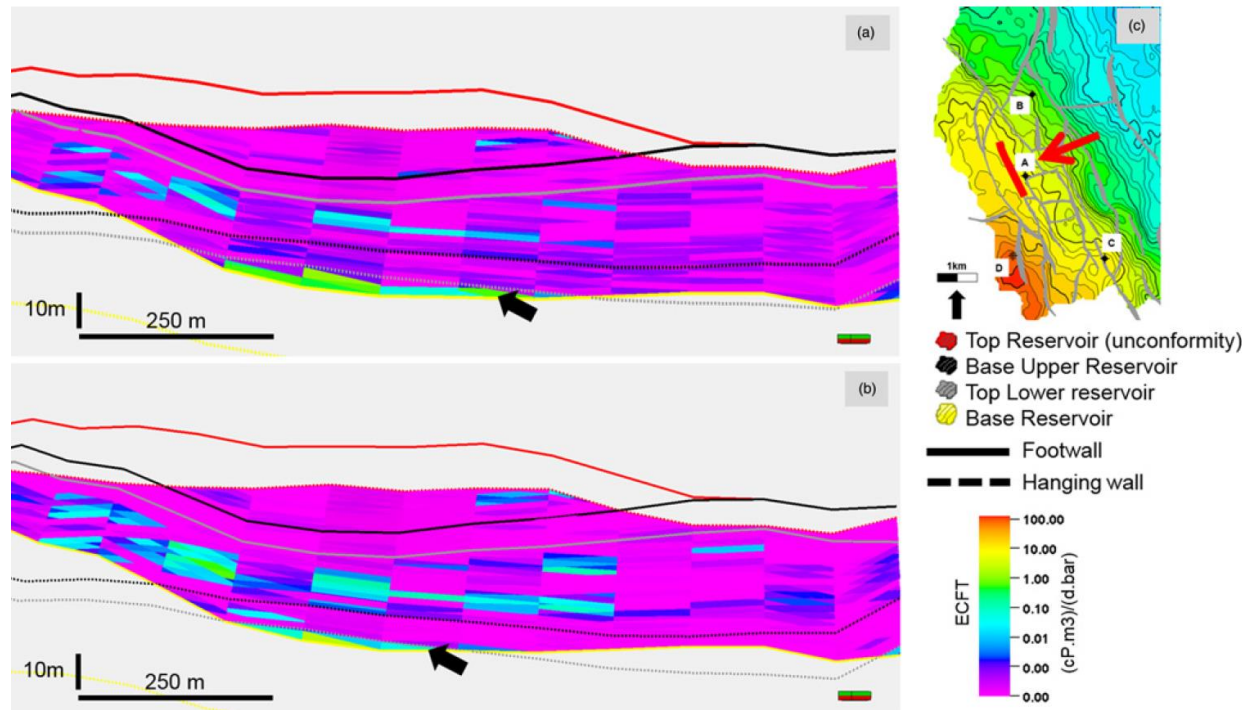


651  
 652 **Fig. 18.** Fault rock permeability versus Vclay from field data (blue squares), measured under  
 653 4000psi with 30% salinity brine and data from an in-house database (shaded areas) measured  
 654 under 70psi and with deionized water as reservoir fluid. Fault rock samples in the in-house  
 655 database are from reservoirs from the same area, the same time and underwent a similar tectonic  
 656 history. (a) Histogram of fault rock Vclay content distribution for the reservoir scale faults.  
 657 Green background = cataclasites/ disaggregation zones, yellow background = phyllosilicate  
 658 framework fault rocks (PFFR), red background = phyllosilicate smear.



659

660 **Fig. 19.** Fault rock permeability versus Vclay from field data (blue squares), measured under  
 661 4000psi with 30% salinity brine and data from an in house database (shaded areas) measured  
 662 under 70psi and with deionized water as reservoir fluid. The data are from burial depths between  
 663 2300m and 3100m, similar to the field data. (a) High, Mid and Low predictive functions for the  
 664 seismic scale faults, using the algorithms from Revil *et al.* (2002). (b) including the fault rock  
 665 permeability prediction curves based on the algorithms from Sperrevik *et al.* (2002) and Jolley *et*  
 666 *al.* (2007).

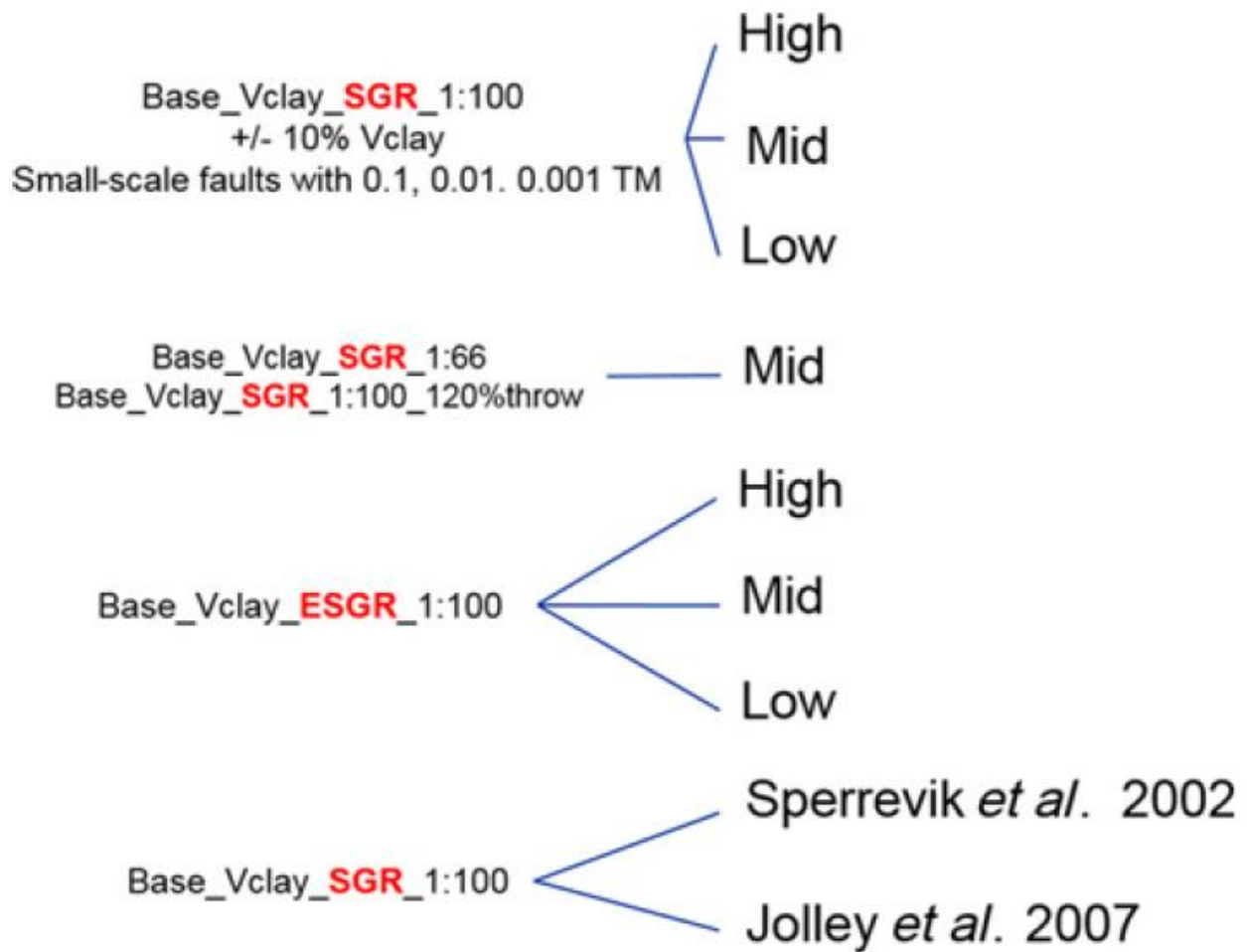


667

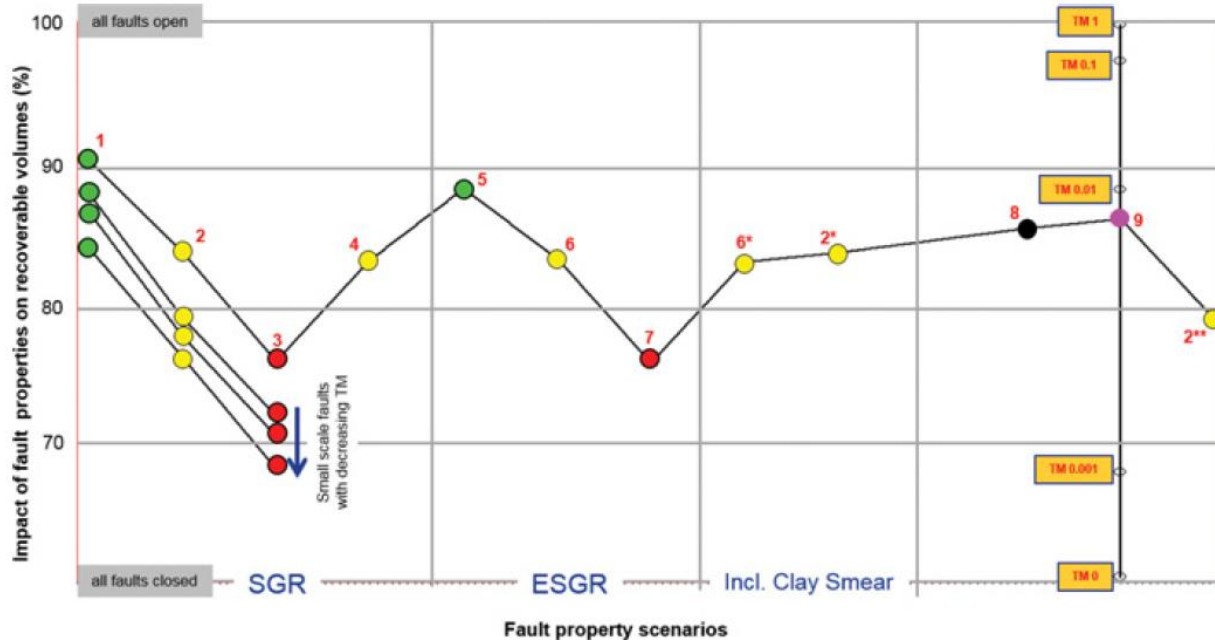
668 **Fig. 20.** Effect of increase in fault throw on ECFT (Freeman *et al.*, 20010). (a) base case throw.

669 (b) 20% increase of fault throw. Note the reduction of the area with high ECFT (black arrow)

670 where the lower reservoir is self-juxtaposed. See discussion in text.



671  
 672 **Fig. 21.** Summary of the scenario for fault rock properties that were run in the dynamic  
 673 simulation model. The “High”, “Mid” and “Low” cases correspond to the three scenarios for  
 674 high, mid and low permeability vs. clay content curves, based on the algorithms from Revil *et al.*  
 675 (2002).



676  
 677 **Fig. 22.** Impact of different fault properties scenarios on recoverable volumes, thickness to throw  
 678 ratio of 1:100, except case 4 with 1:60; 1&5)High\_K, 2&6) Mid\_K, 3&7) Low\_K, 4) Mid\_K with  
 679 thickness to throw ratio of 1:66, 6\* & 2\*) same as case 2 and 6, but taking into account the potential  
 680 of clay smear in addition to the fault gouge, 8) Jolley et al.,2007, 9) Sperrevik et al., 2002, 2\*\*)   
 681 Mid\_K case 2 with 20% increase in throw. Note the impact of incorporating the small scale faults  
 682 on the recoverable volume range. A bulk transmissibility multiplier of 0.1, 0.01 and 0.001 has been  
 683 assigned to the small scale faults. Note that all cases, except 8 and 9 use the mixing algorithms  
 684 from Revil *et al.* (2002) to calculate the fault rock permeabilities. The SGR is used as a fault rock  
 685 Vclay prediction for 8 & 9. The Y-axis is dimensionless.

	Porosity (%)	Permeability (mD)
High	35	5000
Mid	28	50
Low	20	0.5
Clay		0.00028

686  
 687 **Table 1.** Input values for the High, Mid, Low fault rock permeability predictive functions. The  
 688 porosities and permeabilities in the High, Mid and Low rows correspond to the sandstones. Note

689 that these are host rock parameters, which are used in the mixing model proposed by Revil *et al.*  
690 (2002).

691

692

693